NASA TECHNICAL MEMORANDUM

NASA TM X-2010

NASA TM X-2010

FLIGHT INVESTIGATION OF AIRFRAME INSTALLATION EFFECTS ON A VARIABLE FLAP EJECTOR NOZZLE OF AN UNDERWING ENGINE NACELLE AT MACH NUMBERS FROM 0.5 TO 1.3

by Daniel C. Mikkelson and Verlon L. Head

Lewis Research Center
Cleveland, Ohio 44135

NATIONAL AERONAUTICS AND SPACE ADMINISTRATION • WASHINGTON, D. C. • MAY 1970

1. Report No. NASA TM X-2010	2. Government Accession No.	3. Recipient's Catalog No.
4. Title and Subtitle FLIGHT INVESTIGATION OF AIRFRAME INSTALLATION EFFECTS ON A VARIABLE FLAP EJECTOR NOZZLE OF AN UNDERWING ENGINE NACELLE AT MACH NUMBERS FROM 0.5 TO 1.3		5. Report Date May 1970 6. Performing Organization Code
7. Author(s) Daniel C. Mikkelson and Verlon L. Head		8. Performing Organization Report No. E-5467
9. Performing Organization Name and Address Lewis Research Center National Aeronautics and Space Administration Cleveland, Ohio 44135		10. Work Unit No. 720-03 11. Contract or Grant No. 13. Type of Report and Period Covered Technical Memorandum
12. Sponsoring Agency Name and Address National Aeronautics and Space Administration Washington, D.C. 20546		14. Sponsoring Agency Code
15. Supplementary Notes		

16. Abstract

A modified F-106B aircraft with underwing engine nacelles was flight tested to investigate airframe installation effects on a variable flap ejector nozzle. Boattail drag coefficients, nacelle and wing pressures, and boundary-layer measurements were obtained for three 15° conical boattails with projected area equal to 54.8 percent of the nacelle area. Three boattail juncture radii of curvature were tested at nonreheat and at reheat power settings. The installed boattail pressure drag coefficients were lower than isolated nozzle values at subsonic speeds, and boattail transonic drag rise was delayed to Mach 0.97.

17. Key Words *(Suggested by Author(s))*	18. Distribution Statement
Airframe installation effects; Airframe nacelle integration; Propulsion system; Transonic; Flight test; Underwing nacelles; Nozzle installation; Boattail drag; Aircraft component drag; Variable flap ejector nozzle	Unclassified - unlimited

19. Security Classif. (of this report)	20. Security Classif. (of this page)	21. No. of Pages	22. Price*
Unclassified	Unclassified	60	$3.00

*For sale by the Clearinghouse for Federal Scientific and Technical Information
Springfield, Virginia 22151

FLIGHT INVESTIGATION OF AIRFRAME INSTALLATION EFFECTS ON A VARIABLE FLAP EJECTOR NOZZLE OF AN UNDERWING ENGINE NACELLE AT MACH NUMBERS FROM 0.5 TO 1.3

by Daniel C. Mikkelson and Verlon L. Head

Lewis Research Center

SUMMARY

A flight test was conducted using a modified F-106B aircraft with underwing engine nacelles to investigate airframe installation effects on a variable flap ejector nozzle. Boattail drag coefficients, nacelle and wing pressures, and boundary-layer measurements were obtained for three 15° conical boattails with projected area equal to 54.8 percent of the nacelle area. Three boattail juncture radii of curvature were tested at nonreheat and at reheat power settings.

Airframe installation resulted in reduced boattail drag coefficients at subsonic speeds when compared with isolated cold-flow results, and the boattail transonic drag rise was delayed to Mach 0.97. Good agreement existed between flight and 1/20-scale F-106 wind-tunnel model results at all speeds except near Mach 1.0. At subsonic speeds installed boattail drag was less sensitive to boattail juncture radius of curvature than isolated data. The nacelle installation resulted in significant changes in the wing lower surface pressure distribution, and caused a maximum increase in elevon trim of approximately 3.0° at Mach 1.02. Large circumferential variations in nacelle boundary-layer characteristics occurred at all Mach numbers.

INTRODUCTION

As part of a current program in airbreathing propulsion, the Lewis Research Center is investigating airframe installation effects on the performance of exhaust nozzle systems appropriate for use at supersonic speeds. In this program, airframe installation effects are being investigated both in wind tunnel and flight tests at off-design subsonic and transonic speeds.

Recent experience has shown that performance of a nozzle system can be appreci-

ably affected by installation on an aircraft especially at off-design conditions (refs. 1 to 7). With an engine nacelle installation typical of a supersonic cruise aircraft, the nacelle may be installed close to the lower surface of a large wing with the nozzle extending downstream of the wing-trailing edge. This aft location of the nacelle provides shielding of the inlet by the forward wing surface to minimize angle-of-attack effects and may also provide favorable interference between the nacelle and wing. To investigate the effect of the airframe flow field on nozzle performance for a nacelle installation of this type, the Lewis Research Center is conducting a flight test program using a modified F-106B aircraft with underwing engine nacelles. The nacelles house J85-GE-13 afterburning turbojet engines. The F-106B aircraft was selected for this program because it had a delta wing planform and good supersonic performance capability. In this continuing flight program, complex nozzle systems are being investigated in the high subsonic and transonic Mach number range where wind tunnel models are limited to very small sizes to avoid wall interference effects.

The exhaust nozzles reported herein simulated the geometry of a variable flap ejector (VFE) nozzle operating at off-design subsonic and transonic speeds. With this type of nozzle, the required expansion ratio for efficient operation over a wide range in nozzle pressure ratios and flight speeds is obtained by modulating the position of the variable shroud flaps. At high subsonic speeds, for example, the required exit area will be considerably smaller than that required at supersonic cruise. The boattail afterbody that results from this exit-area reduction was simulated in this test by fixed geometry nozzles.

Boattail drag coefficients, nacelle pressures, wing pressures (with and without nacelles installed), and boundary-layer measurements were obtained for a series of VFE nozzles with 15° conical boattail afterbodies. Three boattail juncture radii of curvature were investigated over a Mach number range from 0.5 to 1.3 at nonreheat and at reheat power settings. Results of this test are reported herein, and, in order to evaluate installation effects, comparisons are made with data from both isolated wind tunnel studies (refs. 8 and 9) and results from wind-tunnel investigations of a 1/20-scale F-106 with nacelles that were scaled versions of those flown on the aircraft (refs. 6 and 7).

SYMBOLS

A cross-sectional area of crylindrical nacelle section, 490.9 in.^{2} (3166.9 cm^2)

A_β projected area of boattail, 269.2 in.^{2} (1736.8 cm^2)

b wing span, 457.60 in. (1162.4 cm)

C_{D_β} axial boattail pressure drag coefficient in the direction of the nacelle axis, (Axial force)/$q_0 A$

C_p pressure coefficient, $(p - p_0)/q_0$

D diameter

d nacelle cylindrical diameter, 25.00 in. (63.50 cm)

h pressure altitude

l coordinate defining top of nacelle strut fairing

M Mach number

m_0 mass flow at free-stream conditions through an area equal to the nacelle inlet capture area

m_1 mass flow captured by the nacelle inlet

N exponent in the boundary-layer velocity equation, $V/V_{bl} = (z/\delta)^{1/N}$

P total pressure

p static pressure

q dynamic pressure, $0.7\, p_0 M_0^2$

R radius

r boattail juncture radius of curvature

t coordinate defining wing lower surface at the nacelle semispan location of 32.05 percent

V velocity

w coordinate defining nacelle strut fairing width

x nacelle axial or wing chordwise distance coordinate

y spanwise distance from aircraft centerline

z vertical distance from wing surface or radial distance from nacelle surface

α_0 aircraft angle-of-attack, deg

δ boundary-layer thickness

δ^* boundary-layer displacement thickness

δ^{**} boundary-layer momentum thickness

δ_e elevon deflection angle; + down, - up, deg

τ ratio of secondary total temperature to primary total temperature at station 8

φ nacelle angular coordinate, deg

ω ratio of secondary to primary weight flows at station 8

$\omega\sqrt{\tau}$ corrected secondary weight flow ratio

Subscripts:

bl boundary layer

e effective

ex external

i internal

n nacelle

w wing

0 free-stream or flight condition

1-9 nacelle stations (see fig. 8)

APPARATUS AND PROCEDURE

Aircraft and Nacelles

Figure 1 shows the modified F-106B aircraft in flight with aftmounted underwing engine nacelles. This aircraft is a low, delta wing design with a takeoff gross weight of 41 070 pounds (18 626 kg).

A schematic drawing of the aircraft details and installation of the nacelles is shown in figure 2. The aircraft is 790.40 inches (20.076 m) long and has a 60° sweptback delta planform with a 228.80-inch (5.812-m) semispan. The wing has an approximately 4 percent thick NACA 0004-65 airfoil section with a cambered leading edge. The nacelles were mounted to the wing aft lower surface by two attachment links (which were enclosed by strut fairings) on each side of the fuselage at a spanwise distance (y) of 73.34 inches (1.863 m) or 32.05 percent semispan. Each nacelle houses a J85-GE-13 afterburning turbojet engine. Hereinafter, the nacelles are called left and right, as viewed looking upstream. The VFE nozzles were flown on the left nacelle and a cylindrical reference nozzle was mounted on the right nacelle for all tests except the boundary-layer tests. For these tests, a cylindrical reference nozzle was mounted on both nacelles. The nacelles were installed at a -4.5° incidence angle with respect to the wing chord (fig. 2(b)) in order that the nacelle would be approximately tangent to the wing lower surface near its trailing edge. The nozzles extended aft of the wing trailing edge. The nacelles also extended below the fuselage lower surface which is fairly flat in the region of the nacelles. However, because of transonic area rule considerations, the

fuselage sidewalls on the bottom have a slight contour in the vicinity of the nacelles (fig. 2(a)).

A schematic drawing of the nacelle strut fairings and elevon is shown in figure 3. The narrow nacelle strut fairing (fig. 3(a)) had a maximum width equal to 28.6 percent of the nacelle diameter and was tested with the three VFE nozzles that were investigated. A limited amount of data were obtained with the wide nacelle strut fairing (fig. 3(b)) and the nozzle that had a boattail juncture radius to nacelle cylindrical diameter ratio (radius ratio) of 0.5. This nacelle strut fairing tapered to a maximum width equal to 57.0 percent of the nacelle diameter near the elevon hinge line. Both of the nacelle strut fairing configurations enclosed the two nacelle attachment links. A 24.50-inch (62.23-cm) wide section of each elevon above the nacelles was cut out and fixed to the wing to provide clearance between the movable elevon and nacelle.

A schematic drawing of the nacelle with a typical VFE nozzle is shown in figure 4. The nacelle had a cylindrical diameter d of 25.00 inches (63.50 cm) and was 178.17 inches (452.55 cm) long. The trailing edge of the nozzle extended 0.889 nacelle diameters aft of the wing trailing edge. A normal shock (or pitot) inlet with a 6.1° cowl angle was used. The cowl angle on the lower half of the inlet was slightly higher and faired into a bulged section on the bottom of the nacelle. This faired bulged section was needed to accommodate the J-85 engine accessory package. The nacelle included an interface at either end permitting the testing of various types of inlets and nozzles.

Figure 5 shows a VFE nozzle located under the trailing edge of the F-106 wing, and figure 6 shows the nozzle installed below the fixed elevon cutout with the movable elevon deflected down.

The three fixed-geometry VFE nozzle configurations that were tested are shown in figure 7. All three configurations had boattail angles of 15° with the ratio of boattail projected area to nacelle cross-sectional area (based on the cylindrical diameter) A_{β}/A of 0.548. Boattail juncture radius ratios of 0 (sharp edge), 0.5, and 2.5 were investigated. Since the emphasis of the test was primarily on nozzle boattail pressure drag, simple cylindrical ejectors were used for the nozzle internal geometry. The internal diameter of 16.80 inches (42.67 cm) was sized to provide adequate secondary cooling air during maximum reheat operation and was therefore slightly larger than would be required for subsonic cruise at part power. The J-85 engine had a variable area primary nozzle (fig. 7 and 8) that modulated with changes in power setting. Airflow conditions entering the VFE nozzles were determined from the engine and ejector calibrations of references 10 and 11, respectively.

A schematic drawing of the engine installation in the nacelle is shown in figure 8 along with the nacelle station designation. Secondary cooling air to the nozzle was determined from a calibrated flow valve located near the compressor (ref. 11).

Instrumentation

The aircraft was equipped with a digital data system that multiplexed and recorded quasi-static data on magnetic tape (ref. 12). The data system used Scanivalves to measure pressures and had the capability of measuring 578 parameters. A flight-calibrated test boom located on the aircraft nose was used to determine free-stream static and total pressure along with aircraft angle-of-attack and sideslip angle.

The nacelle was externally instrumented with 22 pressure orifices located at three nacelle angular coordinate stations as shown in figure 9. The nozzles had 12 pressure orifices just ahead of the boattail juncture located at four angular coordinate stations as shown in figure 10. The boattails were instrumented with a total of 90 pressure orifices located at ten angular coordinate stations and at nine axial distance stations. The nine orifices at an angular coordinate station were located such that an equal projected area was assigned to each orifice. These orifices were then used to obtain the boattail axial pressure drag coefficient defined as follows:

$$C_{D_\beta} = -\frac{1}{A}\sum_{i=1}^{90} C_{pi}A_i$$

where C_{pi} is the local boattail pressure coefficient and A_i is the projected area assigned to the i^{th} orifice. For the radius ratio 0 (sharp edge) nozzle, four extra orifices were located at four angular coordinate stations just aft of the sharp boattail juncture. These orifices were used to measure the low pressures that occur with the sharp flow overexpansion at the boattail juncture of this nozzle, and they were not used in determining boattail drag coefficient. The nozzle local ambient pressure P_{9ex} was assumed to be equal to the average pressure measured by the 10 orifices on the boattail trailing edge. The average pressure measured by the eight internal orifices located at the nozzle trailing edge was used as the internal exit static pressure P_{9i}.

Pressure instrumentation which was located on the left wing is shown in figure 11. The upper surface had 36 orifices located at eight axial distance stations and at seven spanwise stations. The lower surface had 40 orifices located at 11 axial distance stations and at six spanwise stations.

Wing and nacelle boundary-layer rake instrumentation details are shown in figure 12. One 10-tube total-pressure rake was located on the wing lower surface inboard of the nacelle as shown in figure 11. Nacelle boundary-layer rake data were obtained at six angular coordinate stations. These rakes were flown at angular coordinates of 45°, 105°, and 165° on both nacelles. However, for convenience, the data are presented as if it all had been obtained with the reference nozzle on the right nacelle. Therefore, an angular coordinate station of 90° is on the outboard side and 270° on the inboard side.

Procedure

Tests were conducted at flight Mach numbers from 0.5 to 1.3 and at Reynolds number that varied from 2.3×10^6 per foot (0.8×10^5 per cm) at Mach 0.5 to 4.4×10^6 per foot (1.4×10^5 per cm) at Mach 1.3. The aircraft was flown at the nominal altitude - Mach number profile shown in figure 13. This altitude profile resulted in the angles-of-attack and the trim elevon deflections shown in figure 14. Tests were conducted at the nozzle pressure ratio schedule shown in figure 15. The nominal nozzle operating conditions and primary diameter ratios for the three J-85 power settings that were investigated are tabulated below. The nacelle inlets were operated at the nominal capture mass flow ratio schedules shown in figure 16 for the corrected secondary to primary weight flow ratios listed in the table.

J-85 power setting	T_8		$\omega\sqrt{\tau}$	D_9/D_{e8}	D_{e8}/d
	^oR	K			
Military	1760	978	0.040	1.45	0.46
Minimum reheat	2480	1378	.040	1.30	.52
Maximum reheat	3550	1972	.065	1.14	.59

RESULTS AND DISCUSSION

Boattail Pressure Drag

Prior to the test reported herein, investigations were conducted in the Lewis Research Center 8- by 6-Foot Supersonic Wind Tunnel with a 1/20-scale model of the F-106 aircraft (refs. 6 and 7). The model had nacelles that were scaled versions of those flown on the aircraft. In these investigations the effects of the nacelle bulged section, angles-of-attack below 8^o, and elevon deflections between $+5^o$ and -5^o on boattail pressure drag coefficient were shown to be small for an installed nacelle with a VFE nozzle. Large variations in inlet capture mass-flow ratio for the main aircraft inlets and the underwing nacelle inlets also had little effect on boattail pressure drag.

All the data presented in this report were obtained with the narrow nacelle strut fairing (fig. 3(a)) unless specifically called out as having been obtained with the wide nacelle strut fairing (fig. 3(b)). Installation effect on boattail pressure drag for the zero radius ratio VFE nozzle operating at a maximum reheat nozzle exit to primary throat diameter ratio of 1.14 is shown in figure 17. To show the installation effect, isolated

wind tunnel data from an 8.5-inch (21.59 cm) diameter cold-flow model and from a 4.0-inch (10.16 cm) diameter model are presented and compared to installed data from the F-106 model and aircraft, and from the 4.0-inch (10.16 cm) diameter model with a simulated wing. The three models had 15° boattails with a zero radius ratio and were tested in the Lewis Research Center 8- by 6-Foot Supersonic Wind Tunnel at a model angle-of-attack of 0°. The 8.5-inch (21.59-cm) diameter cold-flow model had a strut-mounted cylindrical nacelle with a VFE nozzle that was a scaled version of the flight nozzle and is described in reference 8. The data presented for this model were obtained at the nozzle pressure ratio schedule shown in figure 15 for the maximum reheat value of nozzle exit to primary throat diameter ratio at a corrected secondary to primary weight flow ratio of 0.03. This resulted in the nozzle operating with overexpanded flow up to approximately Mach 0.9 and with underexpanded flow above Mach 0.9. The 1/20-scale F-106 model had scaled flow-through nacelles that had cylindrical jet-boundary simulators which were used to approximate the local flow field of a nozzle operating fully expanded over the entire speed range. The data presented for this model were obtained from reference 7. The F-106 flight data were obtained at a maximum reheat power setting where the nozzle operated overexpanded below approximately Mach 1.0 and underexpanded above Mach 1.0 as will be shown later in this report. The 4.0-inch (10.16-cm) diameter model had a cylindrical nacelle with a 10° conical forebody and had a cylindrical jet-boundary simulator. The distance from the cone/cylinder juncture to the boattail trailing edge (in nacelle diameters) was nearly identical to the value for the flight nacelle. In addition to being tested isolated, this model was investigated under a large flat plate at an incidence angle of -4.5° with the boattail trailing edge extending 0.970 nacelle diameter aft of the wing trailing edge as described in reference 9. The installed test with this model was an attempt to investigate installation effects on larger nacelles in the 8- by 6-Foot Supersonic Wind Tunnel with only portions of the wing present.

The boattail drag data presented in figure 17 indicate that an installation of this type resulted in a significant decrease in drag when compared with isolated nacelle results at all speeds except near approximately Mach 1.0. At this speed, flight boattail drag was similar to isolated wind tunnel values indicating little installation effect. The F-106 flight data show that the installed boattail drag coefficients were low at the high subsonic Mach numbers and that the transonic drag rise was delayed to Mach 0.97. Similar results occurred for a number of different nacelle shapes at the same spanwise location (under the F-106) and at a more outboard spanwise location (ref. 7). The flight and wind tunnel installed data compare favorably at all speeds except near Mach 1.0 where the model results underestimate the flight boattail drag. It is also apparent that some of the boattail drag reduction at high subsonic speeds was obtained with just a flat-plate wing simulation, which provided a reflection plate for the nacelle flow field. The further decrease in boattail drag at these speeds for the installed F-106 data was the additional

result of the pressure gradients inherently produced by the lower wing surface curvature.

These installation effects were caused by the acceleration and recompression in the combined flow fields of the wing and nacelle resulting in high pressures on the nozzle afterbody, especially at the high subsonic speeds. These results are qualitatively shown by the nacelle pressure distributions from reference 6 and the wing and nacelle pressure distributions from reference 7. In addition, these results will be supported by the wing and nacelle pressure distributions which will be presented later in this report. Terminal shocks were present on all of the nacelles tested, and they traveled over the boattails at the Mach numbers shown by the dips in the boattail drag coefficient curves of figure 17. However, since tunnel blockage causes a delay in terminal shock travel (refs. 13 and 14), the effects on boattail drag were delayed to approximately Mach 1.02 and 1.08 for the 4.0-inch (10.16-cm) diameter model and the 8.5-inch (21.59-cm) diameter model, respectively.

In addition to the favorable subsonic installation effects, the combined flow fields of the wing and nacelle were shown to be of an oscillatory nature and caused the elevons to vibrate as shown in references 12 and 15. This elevon vibration was obtained only during the flight tests with nacelles installed, at Mach numbers from 0.85 to 1.05, and had a frequency between 45 and 50 hertz with a maximum amplitude at Mach 0.95. During subsequent flight tests with a different nozzle configuration, nacelle strut fairing geometry significantly affected the magnitude of the elevon vibration (ref. 12). The maximum amplitude was reduced to an acceptable level by changing from the narrow nacelle strut fairing of figure 3(a) to the wide strut fairing of figure 3(b).

A comparison of boattail drag data obtained in flight with isolated wind tunnel data for the three radius ratio boattails operating at a maximum reheat nozzle exit to primary throat diameter ratio of 1.14 is shown in figure 18. The isolated cold-flow wind tunnel data (ref. 8) were obtained with the 8.5-inch (21.59-cm) diameter model at a zero degree angle-of-attack for the nozzle pressure ratio schedule of figure 15. Between approximately Mach 1.0 and 1.2 where the data from this model were affected by terminal shock travel, isolated data from the 4.0-inch (10.16-cm) diameter model with a jet-boundary simulator (ref. 9) are also presented for the boattails with radius ratios of 0 and 0.5. The data from this model were obtained at a zero degree angle-of-attack. The effect of increasing the boattail radius ratio from zero (sharp edge) to 2.5 resulted in a large reduction in boattail drag for the isolated boattail at high subsonic speeds. The installation effect, however, resulted in a large reduction in subsonic drag for the zero radius ratio boattail, and increasing the boattail radius ratio to 0.5 and 2.5 had very little additional effects. The drag reduction due to radius ratio was nearly unaffected by installation on the aircraft at supersonic speeds; however, the general level for all three shapes was somewhat less.

The effect of nozzle exit to primary throat diameter ratio on boattail drag is shown in figure 19 for the three radius ratio boattails. The J-85 engine was operated at power settings of military, minimum reheat, and maximum reheat for the nozzle diameter ratios of 1.45, 1.30, and 1.14, respectively. As power setting was increased, the primary nozzle diameter was opened, and generally the size of the primary jet at the nozzle exit increased if the nozzle was not flowing full or greatly overexpanded. The tailed symbols for the boattail with a radius ratio of 0.5 (fig. 19(b)) were obtained with the wide nacelle strut fairing (fig. 3(b)). All other data were obtained with the narrow nacelle strut fairing (fig. 3(a)). A comparison of the data obtained with the two strut fairings at a nozzle diameter ratio of 1.45, showed that boattail drag was not appreciably affected by strut fairing geometry. The effect of increasing power setting resulted in reduced boattail drag for the three radius ratio boattails at all flight speeds. Boattail drag reduction was less sensitive to power setting changes at speeds below Mach 0.97 (where the primary jet was always overexpanded) than at supersonic speeds where the primary jet ranged from overexpanded to underexpanded at nozzle diameter ratios from 1.45 to 1.14, respectively.

The effect of radius ratio on boattail drag is shown in figure 20 for the three nozzle diameter ratios (power settings). At all power settings boattail drag was reduced with increasing radius ratio at supersonic speeds. This reduction was the largest for a radius ratio change from 0.5 to 2.5. However, at subsonic speeds boattail drag was less sensitive to radius ratio.

The effect of nozzle diameter ratio (power setting) on the internal nozzle exit static pressure to free-stream static pressure ratio is shown in figure 21 for the three radius ratio nozzles that were tested. With military and minimum reheat power settings the nozzle pressure ratio schedules and diameter ratios were such that the primary jet was separated at the nozzle exit plane providing approximately free-stream static pressure up to Mach 0.97 and 0.95, respectively. Above these speeds the primary jet overexpands at the nozzle exit to larger effective flow areas except for the radius ratio 0.5 nozzle at minimum reheat power setting above approximately Mach 1.15. Because of the difficulty in repeating minimum reheat power setting, this nozzle was tested at a power setting that was slightly higher than the nominal value for minimum reheat at Mach numbers between 1.05 and 1.30 as shown by the tailed symbols in figure 21(b). Within this speed range, the nozzle diameter ratio varied from 1.26 to 1.28. This was the main factor that caused the nozzle to operate flowing full with an underexpanded primary jet above Mach 1.15. At maximum reheat power setting the primary jet was overexpanded below the speed range from Mach 0.9 to 1.0, and underexpanded above these speeds. The same trends occurred for the nozzle exit static pressure to boattail trailing edge static pressure ratio as shown in figure 22.

Nacelle and Boattail Pressures

A comparison of the flight boattail pressure distributions with isolated nozzle results for the zero radius ratio nozzle operating at a maximum reheat diameter ratio of 1.14 is shown in figure 23. The isolated nozzle data were obtained with the 8.5-inch (21.59-cm) diameter cold-flow model over the nozzle pressure ratio schedule of figure 15 at a 0^{o} angle of attack. The flight data were obtained at aircraft angles of attack that varied with Mach number as shown in figure 14. The electrical signals that were recorded by the aircraft data system for the nacelle pressures obtained during the flight tests of the radius ratio 0 and 2.5 nozzles were subject to a small amount of wide band aircraft electrical noise. This noise caused the measured boattail pressures to vary randomly over the small amplitude range (approximately $\pm 1/4$ lb/in.^{2} (± 0.17 N/cm^2)) shown in figures 23 and 25. Because of the random fluctuation in the boattail pressures, it is difficult to evaluate circumferential variations in these pressures. However, the axial pressure distribution trends and computed boattail drag coefficients are usable because of the small amplitude of the pressure fluctuations and their random variation with time. These pressures fluctuated at relatively high frequencies compared to the data acquisition cycle time of 11.6 seconds. All of the electrical signals for the wing, boattail, and nacelle pressures obtained with the 0.5 radius ratio nozzle were electrically filtered to eliminate this noise.

The installed boattail pressures were generally higher than the isolated nozzle data at both Mach 0.90 and 1.20 as shown in figure 23. These higher installed pressures resulted in the boattail drag coefficient reductions shown in figure 18. At Mach 0.90, the flow on the upper half of the boattail overexpanded at the sharp boattail juncture to pressures that were higher than the minimum obtained with the isolated nozzle. On the lower half of the boattail the opposite trend in general occurred; however, the flow on both the upper and lower halves recompressed to approximately the same pressure level.

A comparison of boattail pressure distributions with isolated nozzle results for the 0.5 radius ratio nozzle operating at a maximum reheat diameter ratio of 1.14 is shown in figure 24. The isolated data shown at Mach 1.05 and 1.10 were obtained with the 4.0-inch (10.16-cm) diameter model with a jet-boundary simulator (ref. 9). At all subsonic Mach numbers the flow overexpansion at the boattail juncture was generally less severe on the upper half of the boattail. The boattail drag reductions due to installation effect shown in figure 18 resulted from the higher average pressures on the boattail (compared with isolated data, fig. 24) at all speeds except Mach 1.00. This trend is particularly clear at Mach 0.95 where the installed boattail pressures were considerably higher than the isolated pressures, and yielded a force in the thrust direction on the boattail. The sharp flow recompression that occurred at Mach 1.20 on the isolated boattail was also evident on the installed boattail, however at a slightly more forward location.

A comparison of boattail pressure distributions with isolated nozzle results for the 2.5 radius ratio nozzle operating at a maximum reheat diameter ratio of 1.14 is shown in figure 25. The scatter in boattail pressures for this nozzle were primarily due to the electrical noise that was discussed earlier. The boattail drag reduction due to installation effect shown in figure 18 at Mach 0.90 occurred primarily on the forward upper half of the boattail as shown in figure 25(a-1). At Mach 1.20 the flow on both the isolated and installed boattails went through a gradual overexpansion and a sharp recompression.

Installed nacelle pressure distributions with the 0.5 radius ratio nozzle operating at a military power diameter ratio of 1.45 are shown in figure 26 for four nacelle angular coordinate stations at speeds from Mach 0.54 to 1.32. These data were obtained at angles-of-attack that varied from 7.7° at Mach 0.54 to 0.9° at Mach 1.32. The pressures on the forward portion of the nacelle demonstrated a similarity to those obtained with typical isolated cone-cylinder nacelle configurations. At subsonic speeds, a typical flow overexpansion occurred when the flow was turned at the inlet-nacelle juncture and the flow recompressed downstream of this location toward free-stream static pressure. Also, the flow on the boattail showed an expansion region at the boattail juncture followed by a recompression, with the aft boattail pressures being recompressed to levels greater than free-stream static. At Mach 0.89 the low pressure levels at the inlet-nacelle juncture, that result from the flow overexpansion, recompressed through a pressure discontinuity region (or terminal shock) that existed between nacelle position coordinate stations of 3.43 and 5.08 (figs. 26 and 27). At Mach 0.96 this pressure discontinuity region moved aft on the nacelle to a position slightly ahead of the boattail. This low pressure region at the inlet-nacelle juncture, that spread in the downstream direction as Mach number was increased from 0.89 to 0.96, and was terminated by a pressure discontinuity region (terminal shock) was possibly caused by a combination of the following two flow phenomena: a reflection of the low pressure inlet-nacelle expansion field by the wing lower surface, and the recompression field inherently produced by the wing lower surface thickness distribution. The rapid rise in the nacelle pressures and associated change in flow characteristics ahead of the boattail at these high subsonic speeds, resulted in the increased boattail pressures (as compared with isolated nozzle data) (figs. 24(b) and (c)), and the reduced boattail drag discussed earlier. Above these speeds, the pressure discontinuity region moved aft of the boattail and the decreased pressures on the boattail resulted in the drag rise observed at Mach 0.97 (fig. 19(b)). At supersonic speeds, the flow recompression on the boattail was not as strong as the recompression at subsonic speeds and the highest pressures on the boattail were always less than free-stream static. Circumferential pressure variations existed over the entire nacelle length. On the forward portion of the nacelle, higher pressures occurred on the bottom of the nacelle, and on the aft portion ahead of the boattail, pressures were

generally higher on the top. Similar results for the nacelle pressure distribution trends were reported in references 6 and 7.

Installed nacelle pressure distributions for the 0.5 radius ratio nozzle operating at a maximum reheat diameter ratio of 1.14 are shown in figure 27 for four nacelle angular coordinate stations at Mach 0.91 and 1.13. The pressure discontinuity region that occurred at approximately Mach 0.90 downstream of a position coordinate station of 3.43 is more clearly seen on this figure than on figure 26. The nacelle pressure distributions obtained with maximum reheat power setting were similar to the distributions obtained with military power setting (fig. 26), except on the aft region of the boattail. With maximum reheat power setting, the flow on the boattail recompressed to higher pressure levels in this region (compared with military power setting data) at both Mach 0.91 and 1.13.

Wing Pressures

The changes in wing static pressures produced by the nacelle installation are shown in figure 28 for the first row inboard of the nacelle at $2y/b = 0.271$. With the nacelle installed, the compression field from the flow turning at the inlet raised the pressures on the wing above the forward half of the inlet at all Mach numbers presented. The flow overexpansion at the inlet-nacelle juncture resulted in a significant low pressure region on the wing at all speeds. This region had its maximum chordwise extent at Mach 1.00 and above and corresponded to the generally low pressures observed at these speeds on the nacelle aft of the inlet-nacelle juncture as shown in figure 26. These modifications to the wing pressure distribution contributed to the transonic elevon trim changes shown in figure 14. At Mach 1.02 a maximum of 3.0° of additional (down) elevon deflection was required to trim the aircraft longitudinally. The low pressure region recompressed to near free-stream static pressure at the wing trailing edge except at Mach 1.00 and above where the recompression occurred downstream of the wing trailing edge.

Wing pressure distributions are shown in figure 29 for all spanwise rows of pressure orifices on both upper and lower surfaces without the nacelle installed. The low pressure regions on both the upper and lower surfaces inherently produced by the wing thickness distribution recompressed toward free-stream static pressure near the wing-trailing edge at Mach numbers below 0.99. An increase in Mach number resulted in lower pressures in this region, and is followed by a stronger recompression further aft on the wing. At Mach 0.99 and above the recompression moves aft of the wing and the pressures remain low to the wing trailing edge. Data are shown in figure 30 with the nacelles installed. Installation of the nacelles had no effect on the wing upper surface

pressures except for changes on the elevon caused by the different elevon position required to keep the airplane trimmed.

The same trends occurred for the lower surface of the wing as previously described for the single row in figure 28. On the lower surface the influence of the nacelle on the pressure distributions diminished with increasing distance outboard of the nacelle.

Boundary-Layer Characteristics

Figures 31 to 33 show the nacelle boundary-layer characteristics for six angular coordinate stations measured at a nacelle station upstream of the nozzle boattail. These data were obtained at angular coordinate stations of 45°, 105°, and 165° on both nacelles with wide strut fairings (fig. 3(b)). However, for convenience the data are presented as if they had been obtained only on the right nacelle. Therefore, angular coordinate stations of 105° and 255° are on the outboard and inboard sides of the nacelle, respectively.

The rakes that were used to survey the nacelle boundary layer were sized to measure approximately twice the boundary-layer thickness predicted by flat-plate theory with a 1/7 power velocity profile. Because of an unusually thick nacelle boundary layer, this sizing actually resulted in rakes that were generally too short. In order to compute displacement and momentum thicknesses, it is necessary to determine the local free-stream velocity (outside of the boundary layer) at each rake location. This velocity could not be generally determined because of the short rakes. However, a velocity based on the local static pressure at each rake and the highest total pressure measured by any tube in the corresponding rake was used as the local free-stream velocity.

Both displacement and momentum thicknesses were computed based on this velocity and an integration out to the tube reading the highest total pressure. Results for the six rakes are shown in figures 31(a) and (b). Also shown in the figure are the values that would be obtained using flat-plate theory with a 1/7 power velocity profile. Results from the boundary-layer calculations show both the displacement and momentum thicknesses to be greater than would be calculated theoretically except for the rakes at nacelle angular coordinate stations of 45° and 315°. However, since the rakes at these two locations extended into the wing boundary layer, the values computed for both the displacement and momentum thicknesses were influenced by this second boundary layer. The values obtained for the other angular coordinate stations showed a considerable amount of circumferential distortion in both displacement and momentum thicknesses that varied with Mach number. At Mach 0.90 the highest values for both displacement and momentum thicknesses occurred on the inboard (255°) and outboard (105°) sides of the nacelle. Figure 31(c) presents the ratio of displacement to momentum thickness. Lines are shown for various boundary-layer form factors ranging from $N = 5$ to 11. The data showed a

spread from a value of $N < 5$ to $N > 11$ with the minimum values occurring at approximately Mach 0.96.

Figure 32 shows boundary-layer velocity profiles for the same six rakes. Velocities are calculated using the measured total pressure and the local static pressure at each rake. Local velocity is then ratioed to the velocity calculated for the tube with the highest total pressure. The profiles for the rakes at nacelle angular coordinate stations of 45° and 315° showed that they are located in a region where the wing boundary layer and the nacelle boundary layer meet. For Mach numbers from 0.6 to 1.2 all the rakes except the one at 45° in general showed various amounts of distortion in their velocity profiles. These velocity profile distortions indicate that there may be some localized flow separation in some regions of the nacelle boundary layer. Figure 33 shows nacelle boundary-layer velocity data at Mach 0.9. In this figure the ordinate is the radial distance from the surface divided by the boundary-layer thickness. Presenting the data in this way showed that the greatest deviation from the 1/7 power profile occurred in the midregion of the boundary layer where the profile was the most highly distorted.

Figures 34 to 36 show wing lower surface boundary-layer characteristics determined from measurements taken by a rake located between the nacelle and aircraft fuselage. The exact location of this rake is shown in figure 11 and the rake dimensions in figure 12. Figures 34(a) and (b) show both the displacement and momentum thicknesses to be lower than that calculated using flat-plate theory with a 1/7 power profile. Both values are the closest to flat-plate theory at approximately Mach 0.85. Figure 34(c) shows the ratio of displacement to momentum thickness to be less than that predicted for a 1/7 power profile except from approximately Mach 0.85 to 1.00. Figure 35 shows typical velocity profiles from Mach 0.6 to 1.2, and figure 36 shows a typical velocity profile at Mach 0.9 compared with a 1/7 power velocity profile. The wing boundary layer exhibited no separation and generally agreed better with flat-plate theory than the nacelle boundary-layer results.

SUMMARY OF RESULTS

To study airframe installation effects on a variable flap ejector nozzle at subsonic and transonic speeds, a flight test investigation was conducted using a modified F-106B aircraft with underwing engine nacelles. Boattail drag coefficients, nacelle pressures, wing pressures, and boundary-layer measurements were obtained for a series of nozzles with 15° conical boattail afterbodies. Three boattail juncture radii of curvature were investigated over a Mach number range from 0.5 to 1.3 at nonreheat and at reheat power settings. The following results were obtained:

1. Airframe installation effects resulted in reduced boattail drag at all Mach num-

bers except near Mach 1.0. At this speed, flight boattail drag was similar to isolated wind tunnel values indicating little installation effect.

2. Good agreement existed between the flight and F-106 model results at all speeds except near Mach 1.0 where the model results underestimated the flight boattail drag.

3. Installation effects were caused by changes in the nozzle flow field characteristics that resulted from the acceleration and recompression of the combined wing/nacelle flow field at high subsonic Mach numbers.

4. Installed boattail drag at subsonic Mach numbers was less sensitive to boattail juncture radius ratio than isolated data.

5. Boattail drag was reduced with increasing primary nozzle area (increased afterburning) above Mach 1.0. Below Mach 0.97 the same trend occurred, however, the boattail drag reduction was less sensitive to jet characteristics.

6. The nacelle installation resulted in significant changes in the wing lower surface pressure distribution. These changes in the wing pressure distribution contributed to a maximum increase in required (down) elevon trim of approximately 3.0° at Mach 1.02.

7. Large circumferential variations in nacelle boundary-layer characteristics occurred at all Mach numbers.

Lewis Research Center,
National Aeronautics and Space Administration,
Cleveland, Ohio, January 21, 1970,
720-03.

REFERENCES

1. Corson, Blake W., Jr.; and Schmeer, James W.: Summary of Research on Jet-Exit Installation. NASA TM X-1273, 1966.

2. Runckel, Jack F.: Jet-Exit and Airframe Interference Studies on Twin-Engine-Fuselage Aircraft Installations. NASA TM X-1274, 1966.

3. Runckel, Jack F.; Lee, Edwin E., Jr.; and Simonson, Albert J.: Sting and Jet Interference Effects on the Afterbody Drag of a Twin-Engine Variable-Sweep Fighter Model at Transonic Speeds. NASA TM X-755, 1963.

4. Nichols, Mark R.: Aerodynamics of Airframe-Engine Integration of Supersonic Aircraft. NASA TN D-3390, 1966.

5. Blaha, Bernard J.; Mikkelson, Daniel C.; and Harrington, Douglas E.: Wind Tunnel Investigation of Installation Effects on Underwing Supersonic Cruise Exhaust Nozzles at Transonic Speeds. NASA TM X-52604, 1969.

6. Blaha, Bernard J.; and Mikkelson, Daniel C.: Wind Tunnel Investigation of Airframe Installation Effects on Underwing Engine Nacelles at Mach Numbers from 0.56 to 1.46. NASA TM X-1683, 1968.

7. Blaha, Bernard J.: Effect of Underwing Engine Nacelle Shape and Location on Boattail Drag and Wing Pressures at Mach Numbers from 0.56 to 1.46. NASA TM X-1979, 1970.

8. Harrington, Douglas E.: Jet Effects on Boattail Pressure Drag of Isolated Ejector Nozzles at Mach Numbers from 0.60 to 1.47. NASA TM X-1785, 1969.

9. Harrington, Douglas E.: Effect of a Rectangular Simulated Wing on the Pressure-Drag Coefficient of Various Boattails at Mach Numbers from 0.60 to 1.47. NASA TM X-52609, 1969.

10. Antl, Robert J.; and Burley, Richard R.: Steady-State Airflow and Afterburning Performance Characteristics of Four J85-GE-13 Turbojet Engines. NASA TM X-1742, 1969.

11. Samanich, Nick E.; and Huntley, Sidney C.: Thrust and Pumping Characteristics of Cylindrical Ejectors Using Afterburning Turbojet Gas Generator. NASA TM X-52565, 1969.

12. Crabs, Clifford C.; Mikkelson, Daniel C.; and Boyer, Earle O.: An Inflight Investigation of Airframe Effects on Propulsion System Performance at Transonic Speeds. Presented at the 13th Annual Symposium of the Society of Experimental Test Pilots, Los Angeles, Calif., Sept. 25-27, 1969.

13. Mitchell, Glenn A.: Blockage Effects of Cone-Cylinder Bodies on Perforated Wind Tunnel Wall Interference. NASA TM X-1655, 1968.

14. Blaha, Bernard J.; and Bresnahan, Donald L.: Wind Tunnel Installation Effects on Isolated Afterbodies at Mach Numbers from 0.56 to 1.5. NASA TM X-52581, 1969.

15. Wilcox, Fred A.; Samanich, Nick E.; and Blaha, Bernard J.: Flight and Wind Tunnel Investigation of Installation Effects on Supersonic Cruise Exhaust Nozzles at Transonic Speeds. Paper 69-427, AIAA, June 1969.

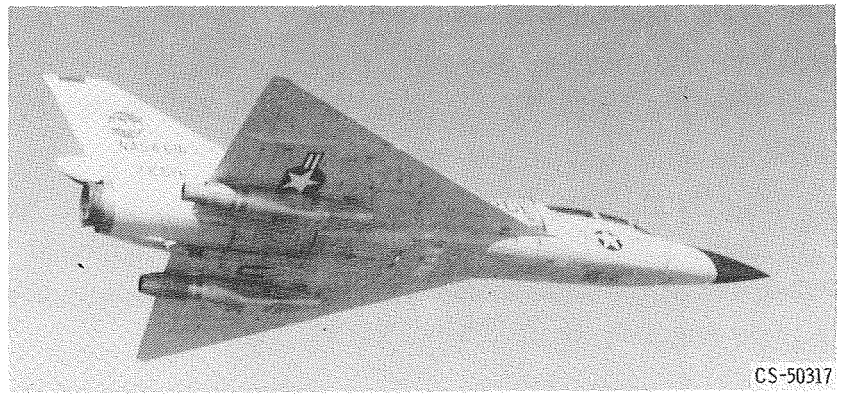

Figure 1. - Modified F-106B aircraft in flight showing under-wing installation of nacelles.

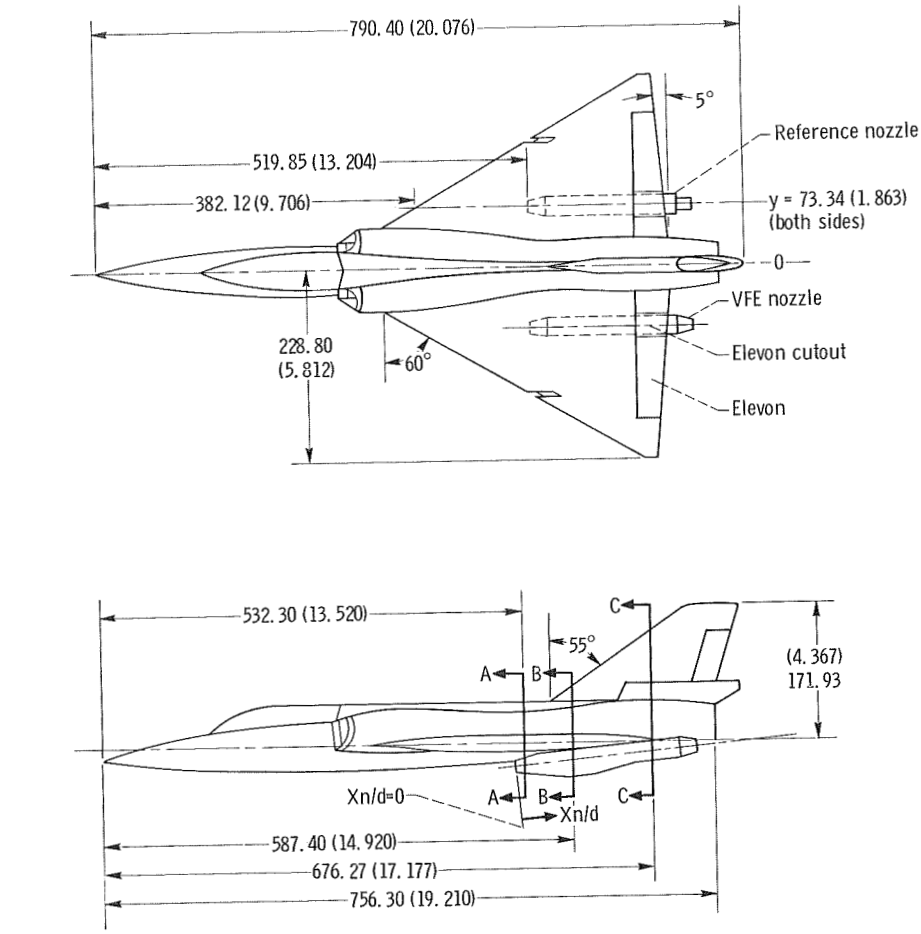

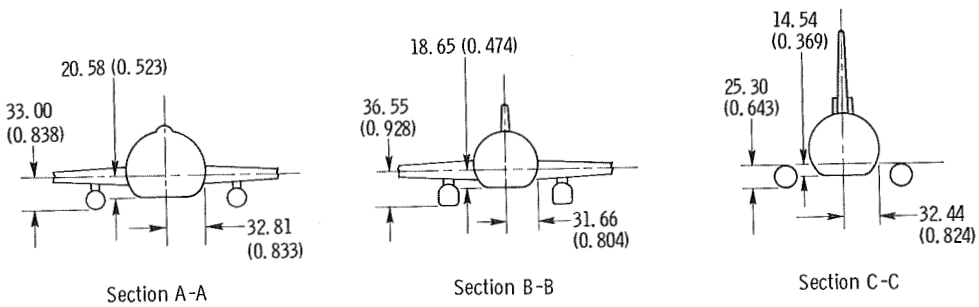

(a) Aircraft details.

Figure 2. - Aircraft details and installation of nacelles under the wing (dimensions are in inches (m)).

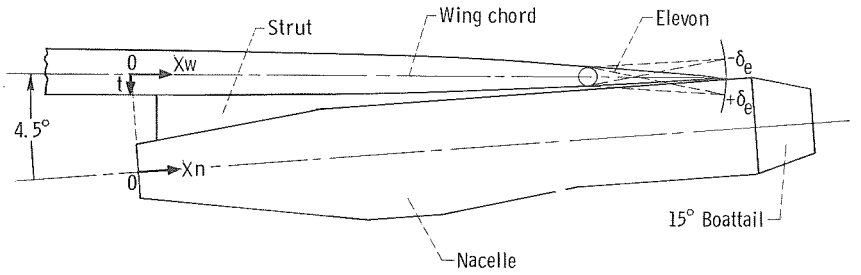

Wing lower-surface coordinates			
X_w/d	t/d	X_w/d	t/d
0	0.225	3.613	0.166
.338	.226	4.202	.145
1.069	.225	4.754	.107
2.282	.218	5.402	.062
2.802	.196	6.257	.004

(b) Nacelle installation.

Figure 2. - Concluded.

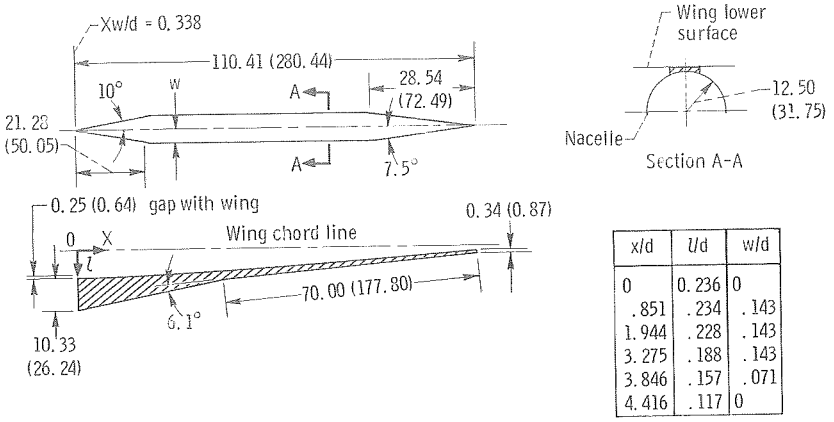

x/d	l/d	w/d
0	0.236	0
.851	.234	.143
1.944	.228	.143
3.275	.188	.143
3.846	.157	.071
4.416	.117	0

(a) Narrow nacelle strut fairing.

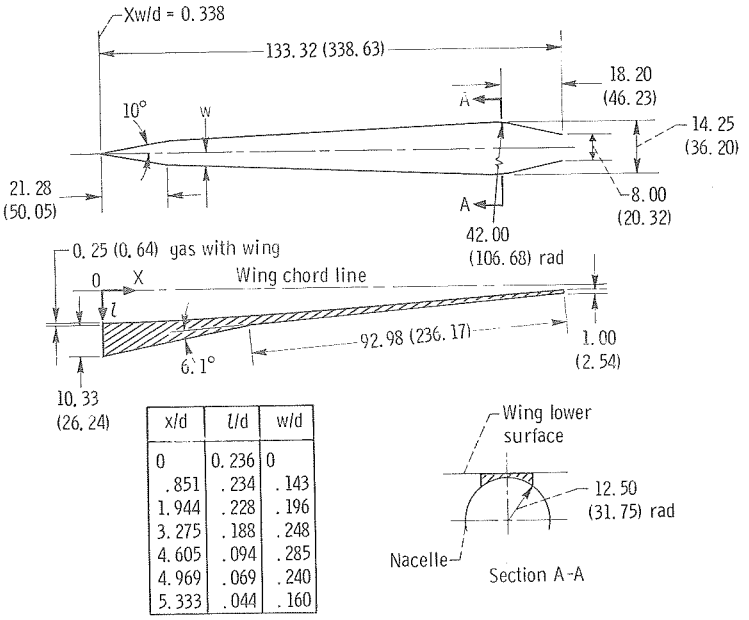

x/d	l/d	w/d
0	0.236	0
.851	.234	.143
1.944	.228	.196
3.275	.188	.248
4.605	.094	.285
4.969	.069	.240
5.333	.044	.160

(b) Wide nacelle strut fairing.

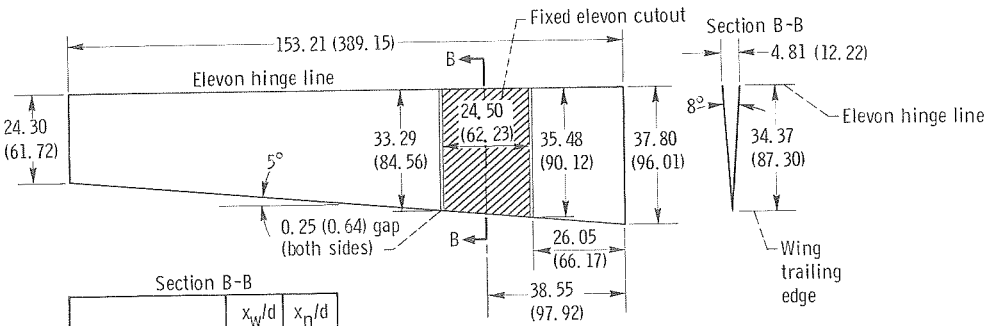

Section B-B

	x_w/d	x_n/d
Elevon hinge line	4.912	4.945
Wing trailing edge	6.290	6.240

(c) Elevon.

Figure 3. - Nacelle strut fairings and elevon. (Dimensions are in inches (cm).)

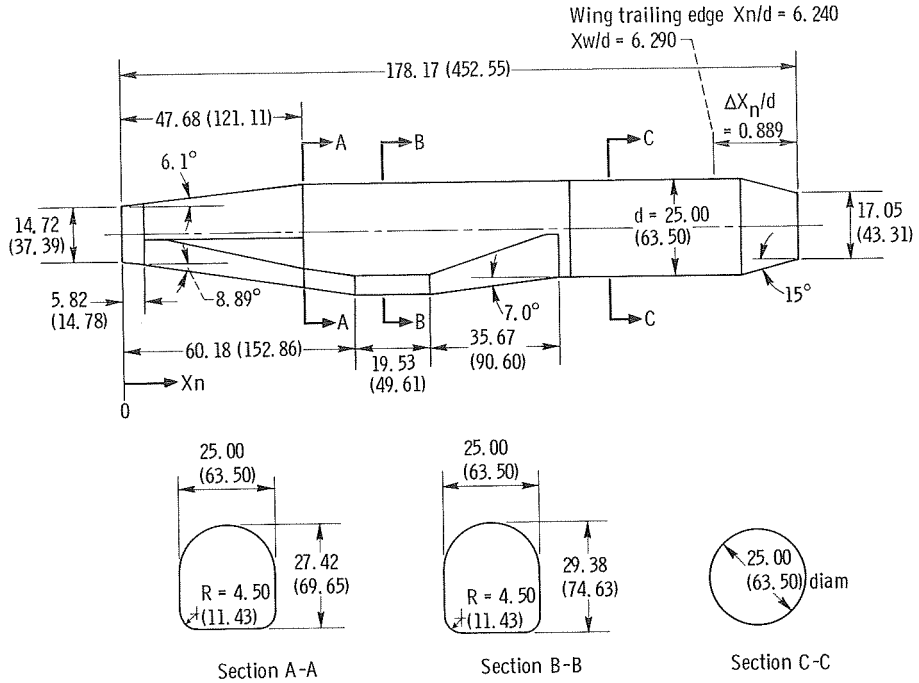

Figure 4. - Nacelle. (Dimensions are in inches (cm).)

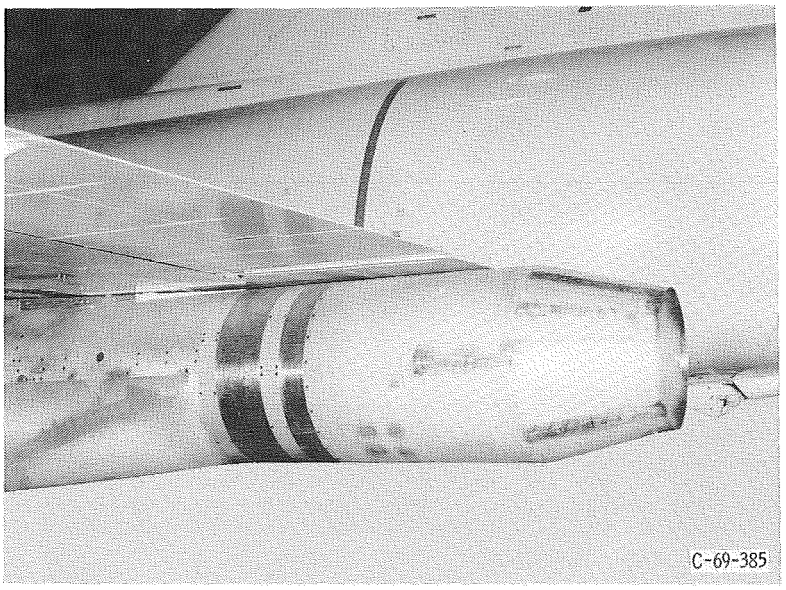

Figure 5. - Variable flap ejector nozzle location under the trailing edge of the wing.

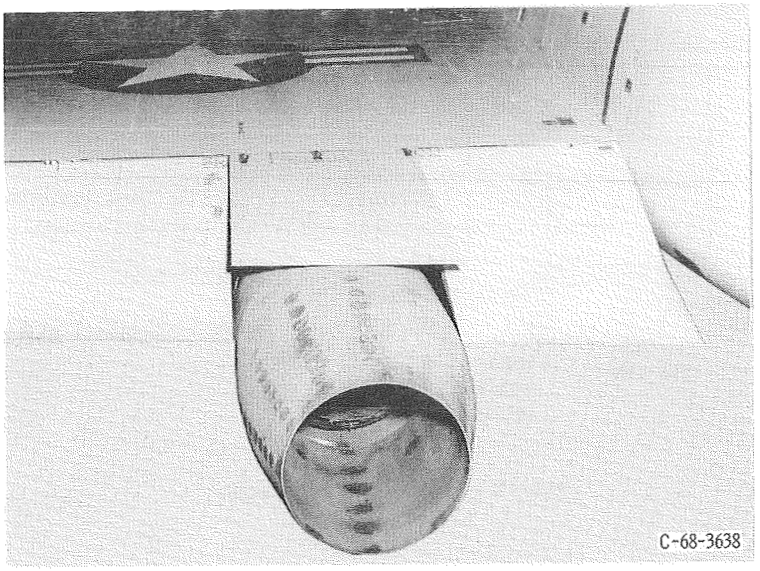

Figure 6. - Variable flap ejector nozzle showing the elevon cutout area with the elevons deflected down.

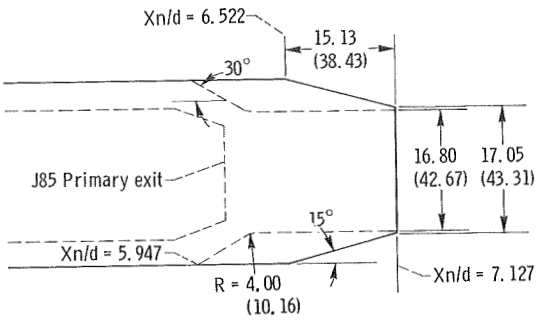

(a) Radius ratio, 0.

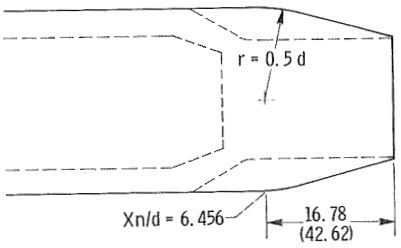

(b) Radius ratio, 0.5.

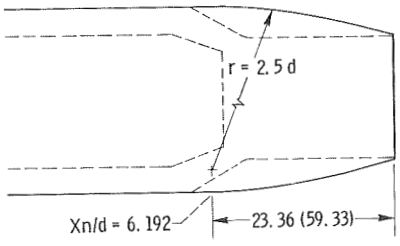

(c) Radius ratio, 2.5.

Figure 7. - Variable flap ejector nozzle geometry details. (dimensions are in inches (cm).)

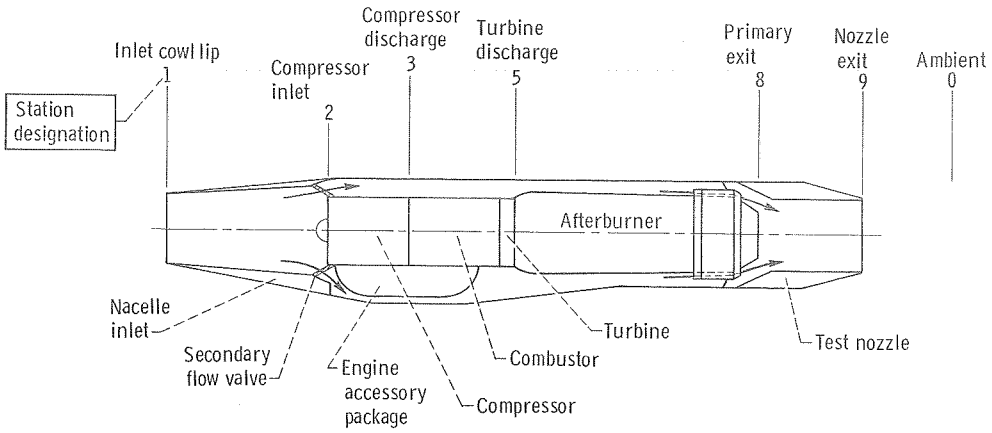

Figure 8. - Engine installation in nacelle.

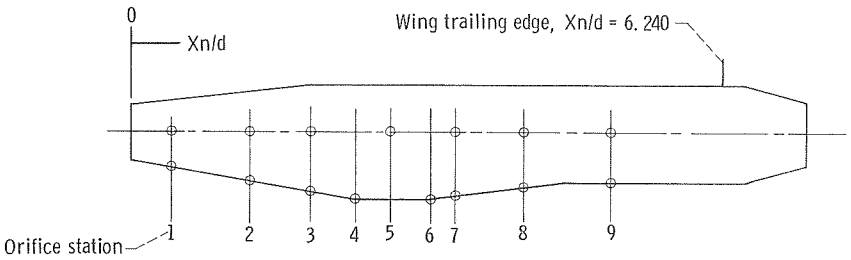

Orifice location on nacelle	Orifice station	Nondimensional position coordinate, x_n/d	Nacelle angular coordinate, φ, deg
Conic forebody	1	0.407	90, 180, 270
	2	1.259	↓
	3	2.047	
Nacelle body	4	2.367	180
	5	2.727	90, 270
	6	2.967	180
	7	3.427	90, 180, 270
	8	4.147	↓
	9	5.067	

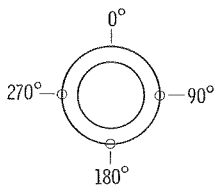

Upstream view

Figure 9. - Nacelle external static pressure instrumentation.

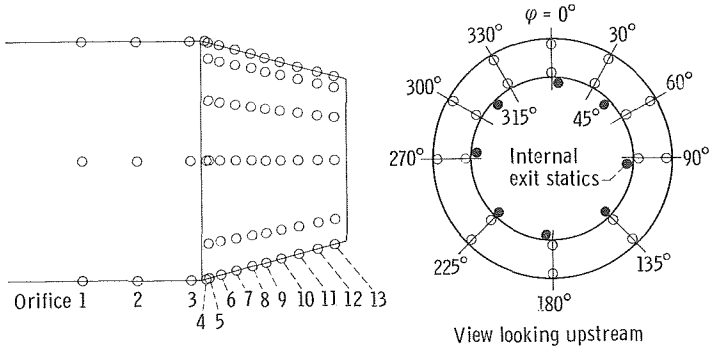

Orifice location on nozzle	Orifice station	Nondimensional position coordinate, x_n/d			Nozzle angular coordinate, φ, deg
		Nozzle radius ratio, r/d			
		0	0.5	2.5	
Nozzle forebody	1	6.042	6.042	5.627	0, 90, 180, 270
	2	6.262	6.262	5.887	↓
	3	6.482	6.482	6.187	↓
Boattail shoulder location	--	6.522	6.456	6.192	----------
Boattail	4	6.535	-----	-----	0, 90, 180, 270
	5	6.549	6.542	6.386	0, 30, 60, 90, 135, 180, 225, 270, 300, 330
	6	6.607	6.607	6.529	↓
	7	6.666	6.666	6.630	↓
	8	6.727	6.727	6.714	↓
	9	6.790	6.790	6.788	↓
	10	6.856	6.856	6.856	↓
	11	6.926	6.926	6.926	↓
	12	6.998	6.998	6.998	↓
	13	7.075	7.075	7.075	↓
Internal exit statics	--	7.107	7.107	7.107	0, 45, 90, 135, 180, 225, 270, 315

Figure 10. - Nozzle static pressure instrumentation.

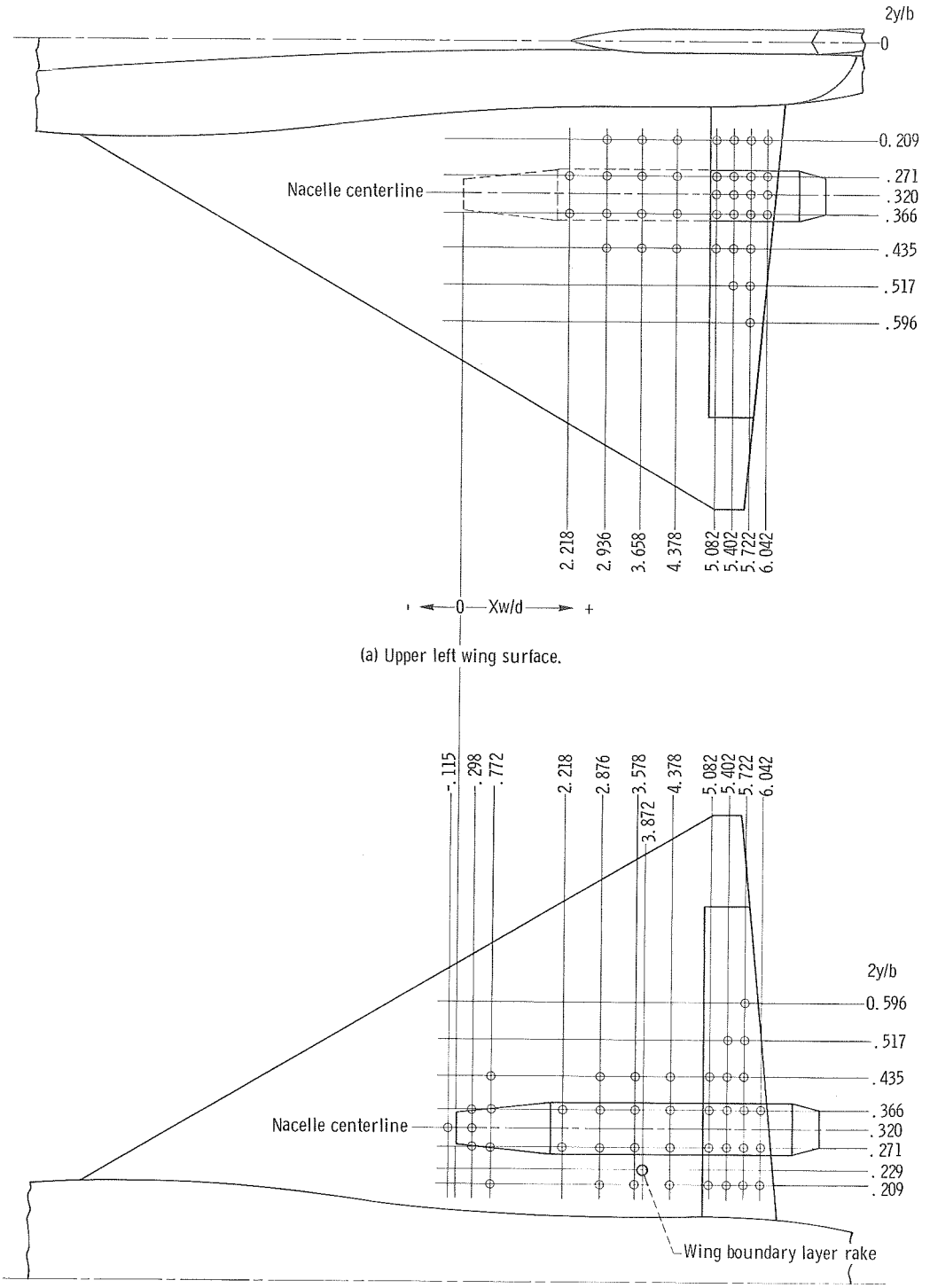

Figure 11. - Wing pressure instrumentation details and coordinate references.

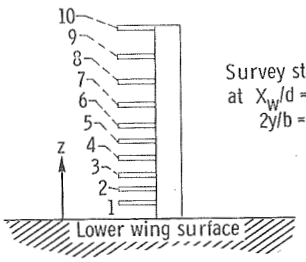

Tube	z/d
1	0.0076
2	.0148
3	.0248
4	.0372
5	.0520
6	.0696
7	.0892
8	.1116
9	.1364
10	.1608

(a) Wing boundary-layer rake instrumentation.

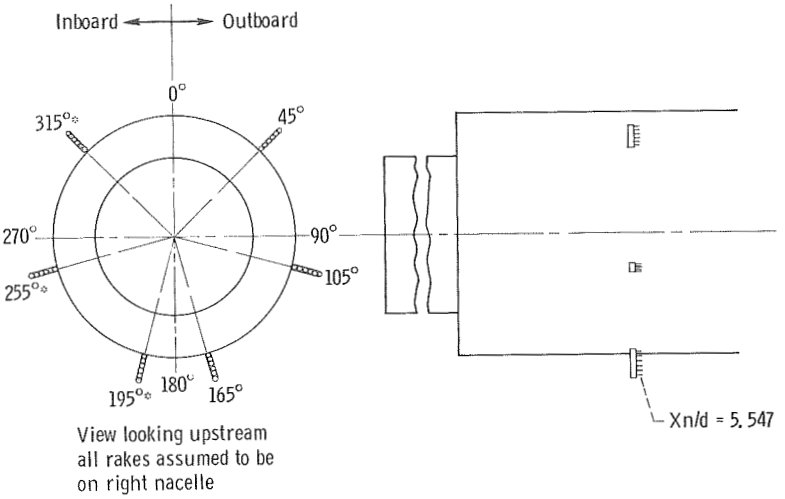

Asterisks denote rakes tested on inboard side of left nacelle

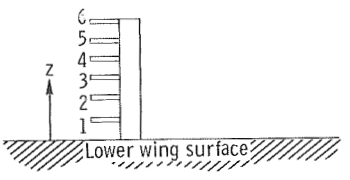

Tube	z/d
1	0.0060
2	.0172
3	.0344
4	.0568
5	.0848
6	.1200

(b) Nacelle boundary-layer rake instrumentation.

Figure 12. - Boundary-layer instrumentation details.

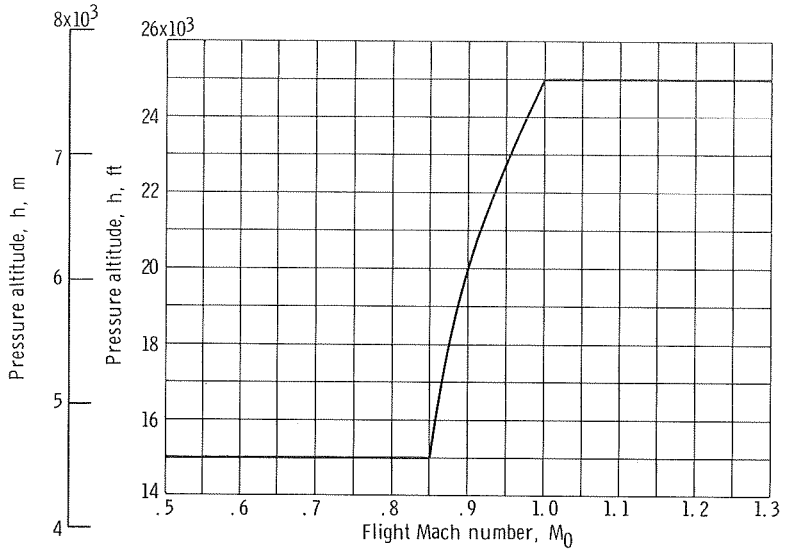

Figure 13. - Nominal flight test altitude-Mach number profile.

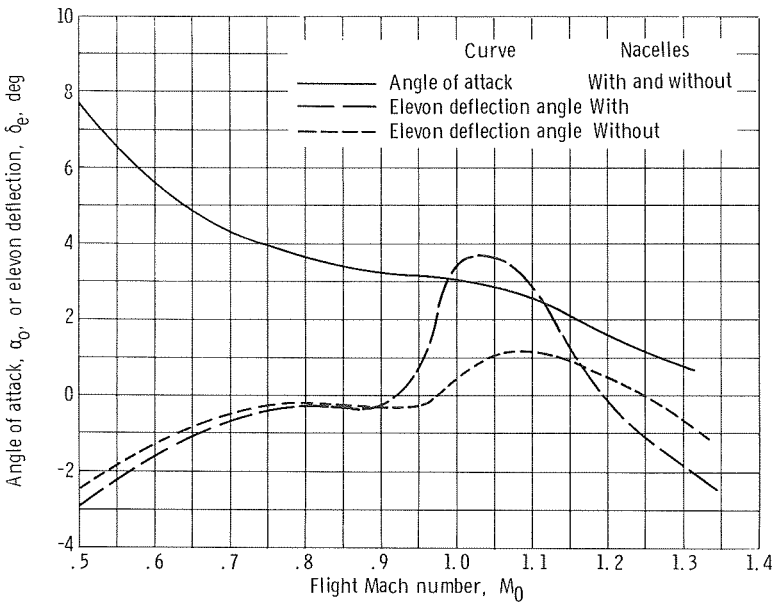

Figure 14. - Comparison of angle-of-attack and elevon deflection with and without nacelles installed.

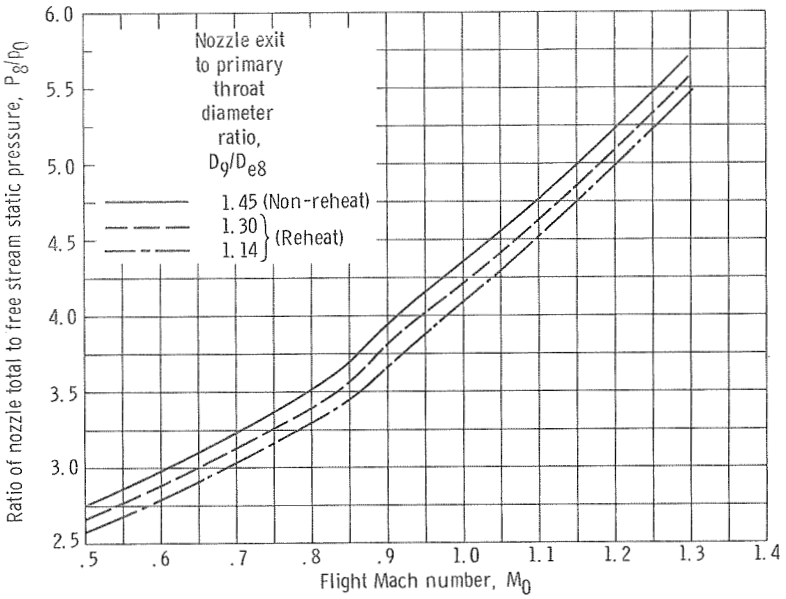

Figure 15. - Nozzle pressure ratio schedule.

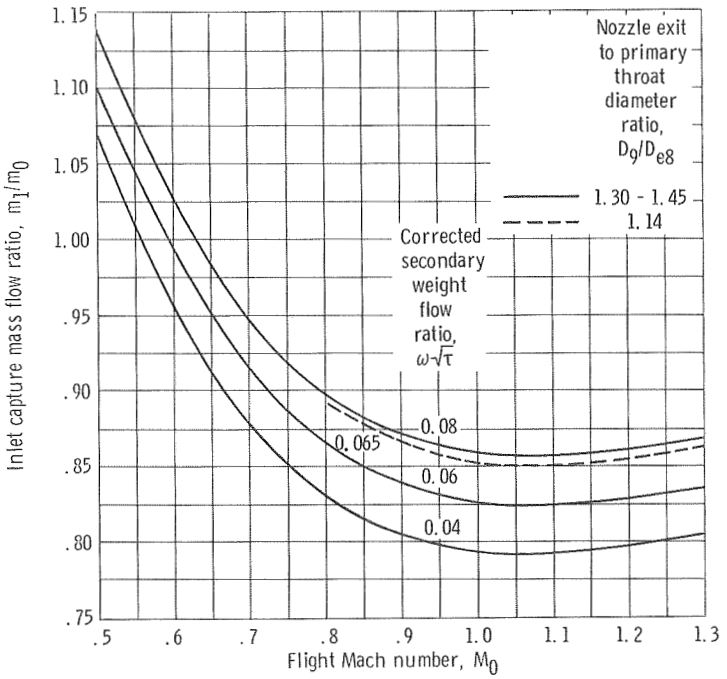

Figure 16. - Nominal inlet capture mass flow ratio schedule.

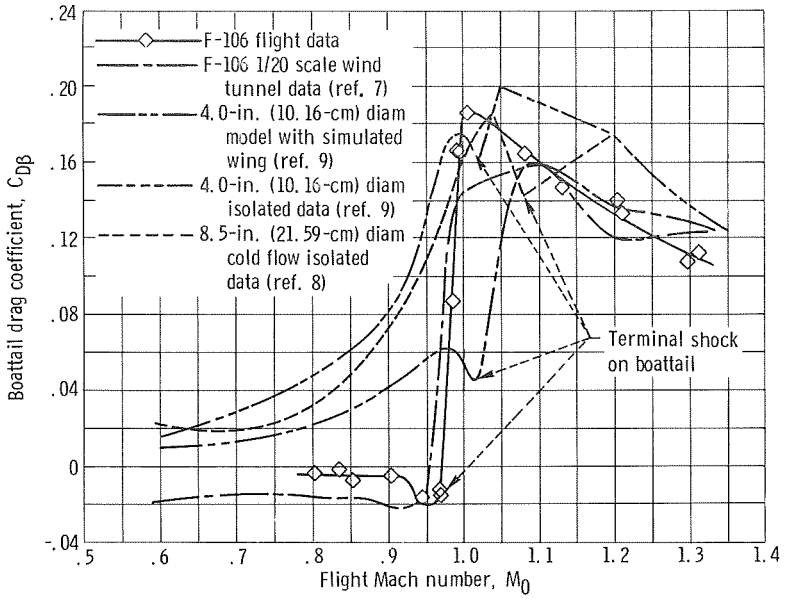

Figure 17. - Installation effect on boattail drag coefficient. Radius ratio, 0; nozzle exit to primary throat diameter ratio, 1.14.

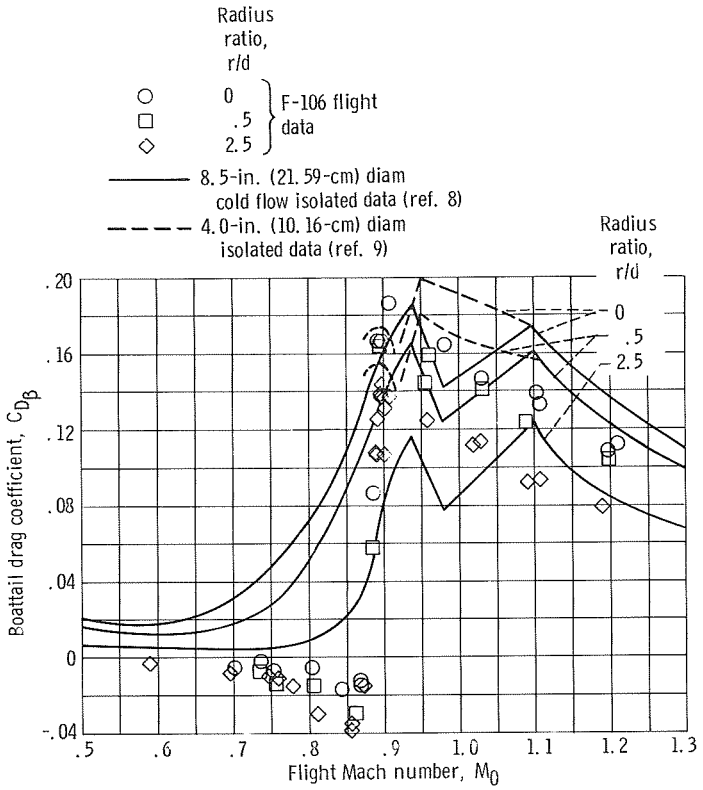

Figure 18. - Comparison of flight data with isolated wind tunnel data for three boattail juncture radius ratios. Nozzle exit to primary throat diameter ratio, 1.14.

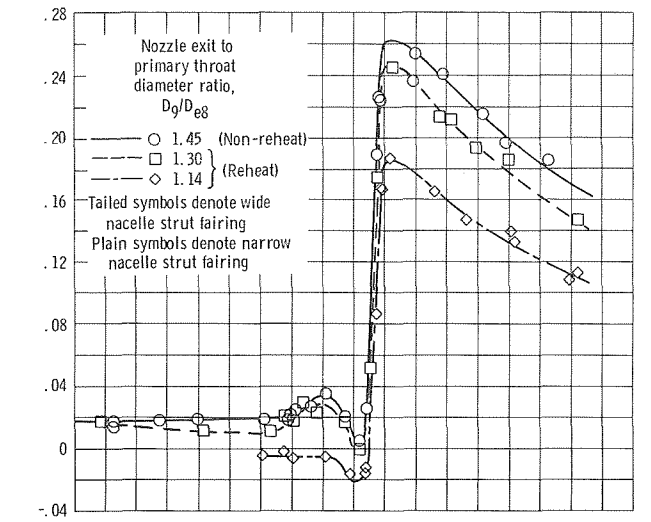

(a) Radius ratio, 0.

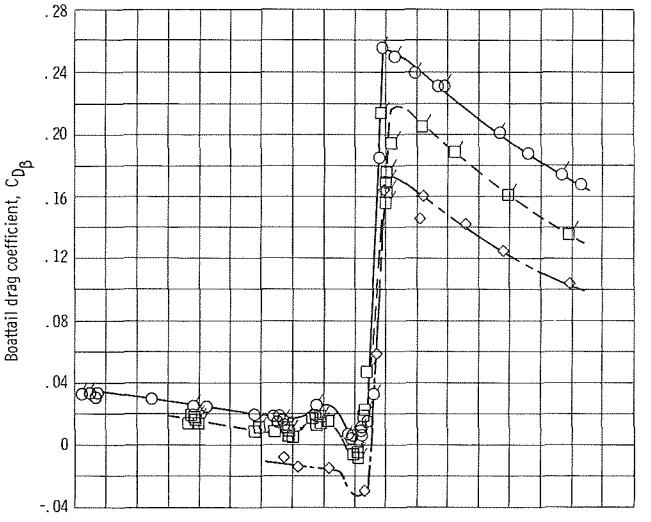

(b) Radius ratio, 0.5.

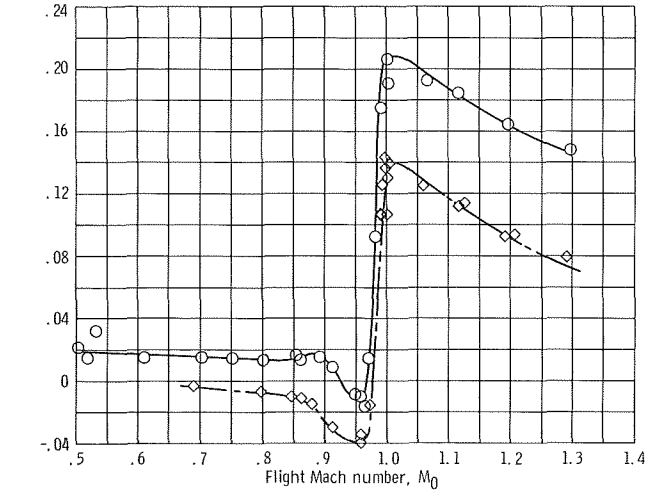

(c) Radius ratio, 2.5.

Figure 19. - Effect of nozzle exit to primary throat diameter ratio on boattail drag coefficient.

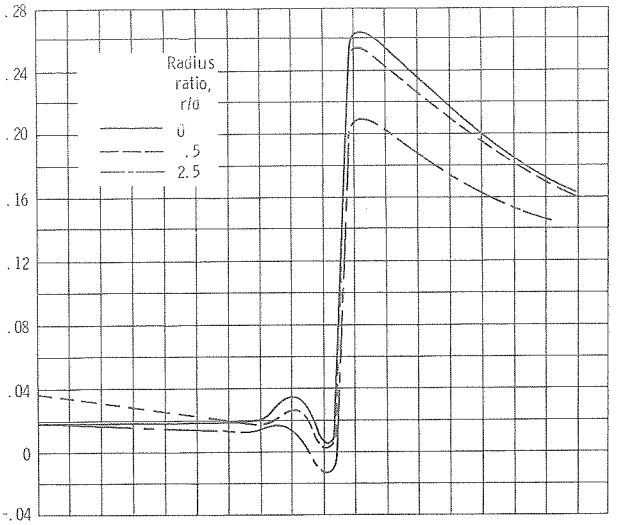

(a) Nozzle exit to primary throat diameter ratio, 1.45.

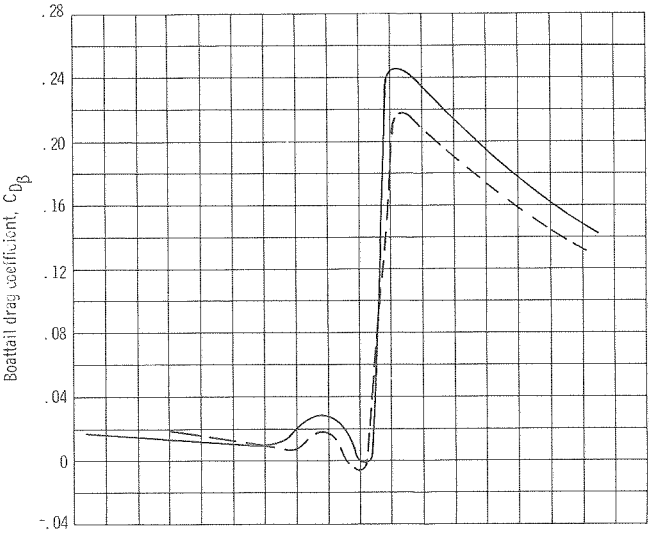

(b) Nozzle exit to primary throat diameter ratio, 1.30.

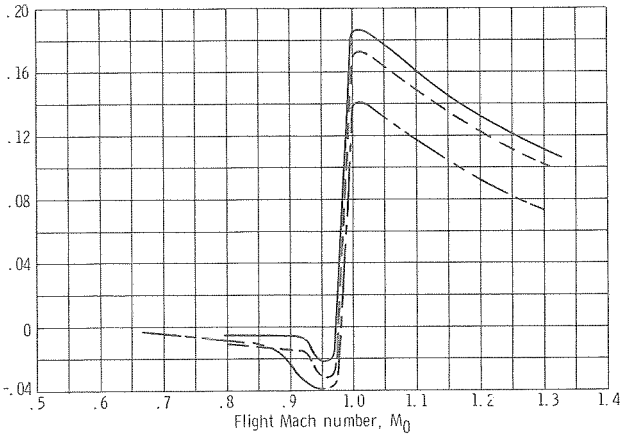

(c) Nozzle exit to primary throat diameter ratio, 1.14.

Figure 20. - Effect of boattail juncture radius ratio on boattail drag coefficient.

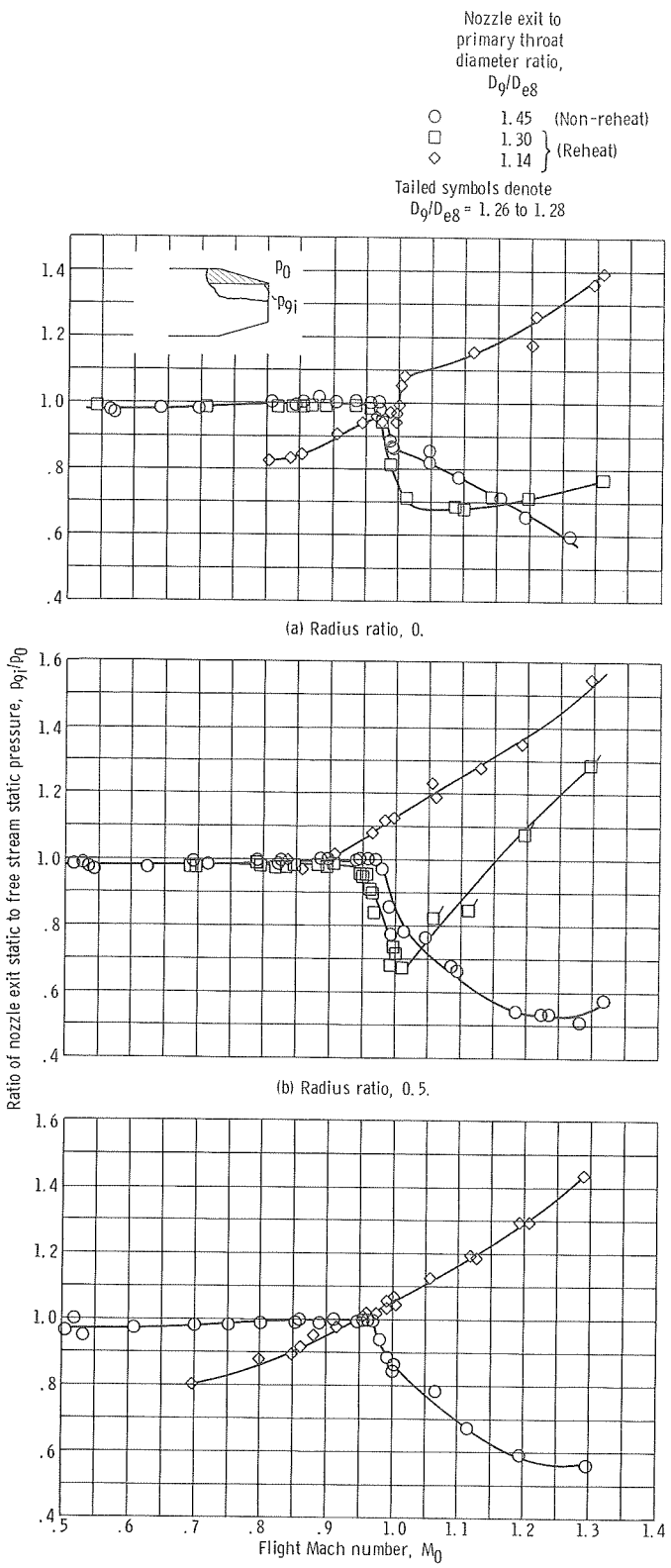

(a) Radius ratio, 0.

(b) Radius ratio, 0.5.

(c) Radius ratio, 2.5.

Figure 21. - Effect of nozzle exit to primary throat diameter ratio on nozzle exit to free-stream static pressure ratio.

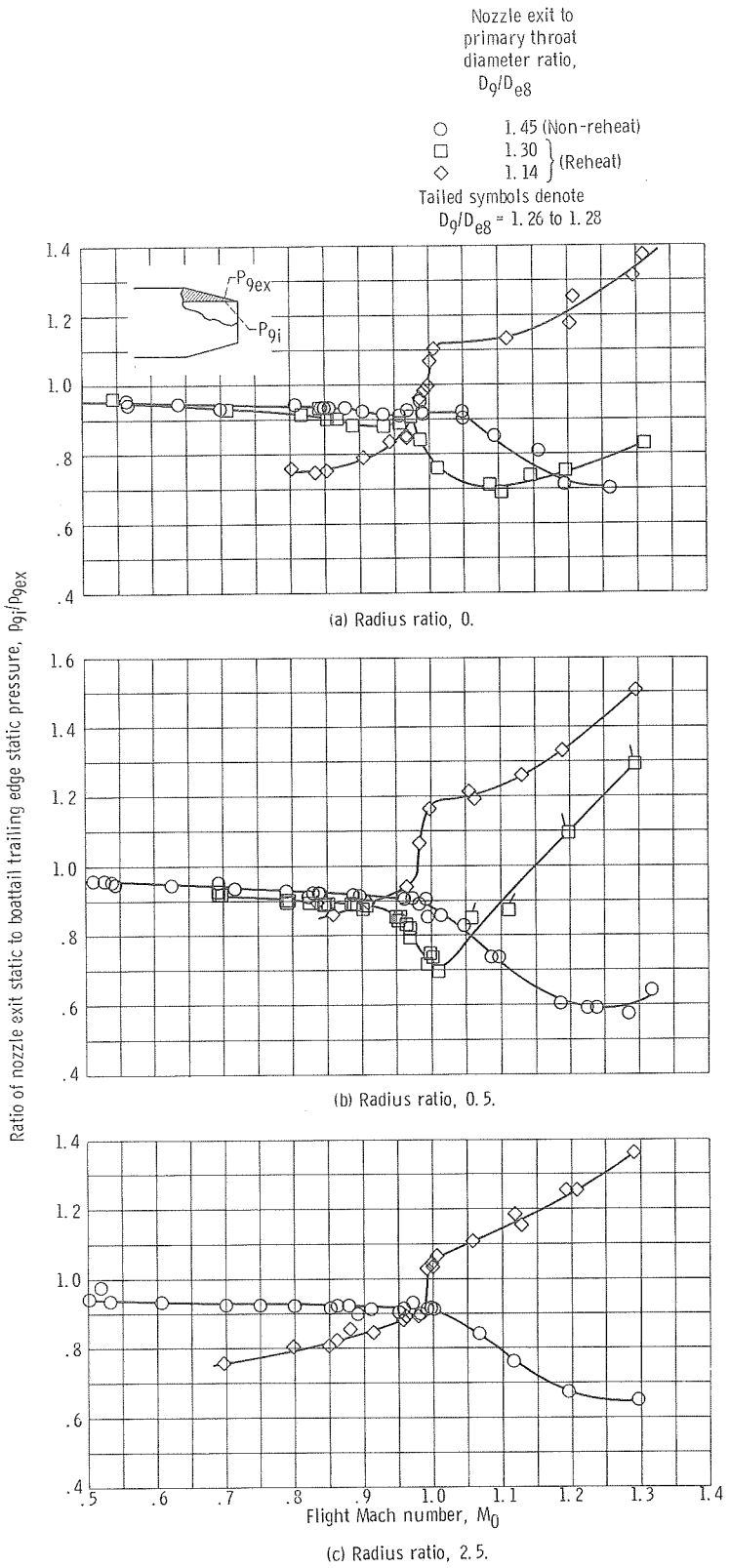

Figure 22. - Effect of nozzle exit to primary throat diameter ratio on nozzle exit to boat-tail trailing-edge static-pressure ratio.

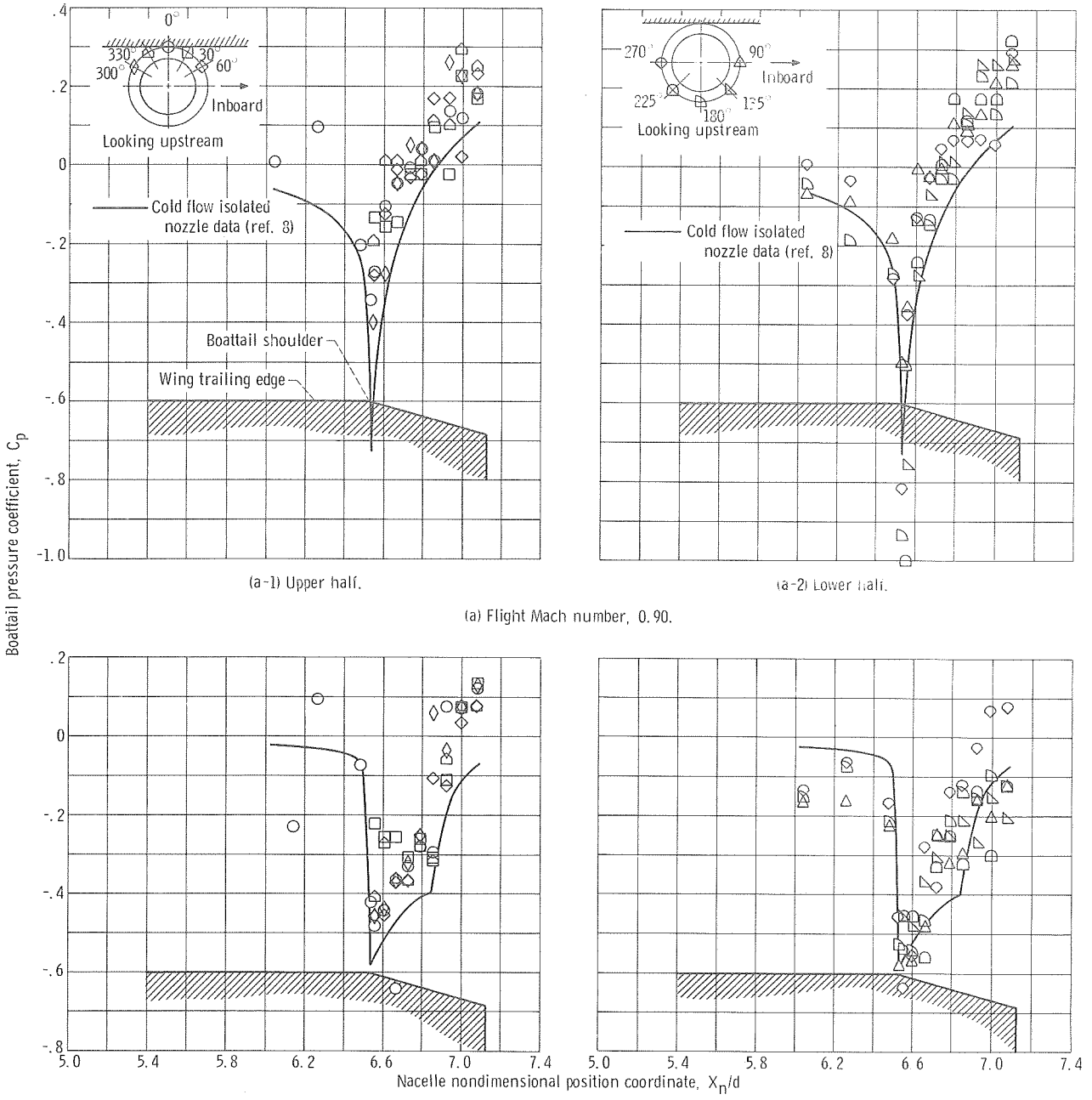

Figure 23. - Comparison of boattail pressure distribution with isolated nozzle data. Radius ratio, 0; nozzle exit to primary throat diamter ratio, 1.14.

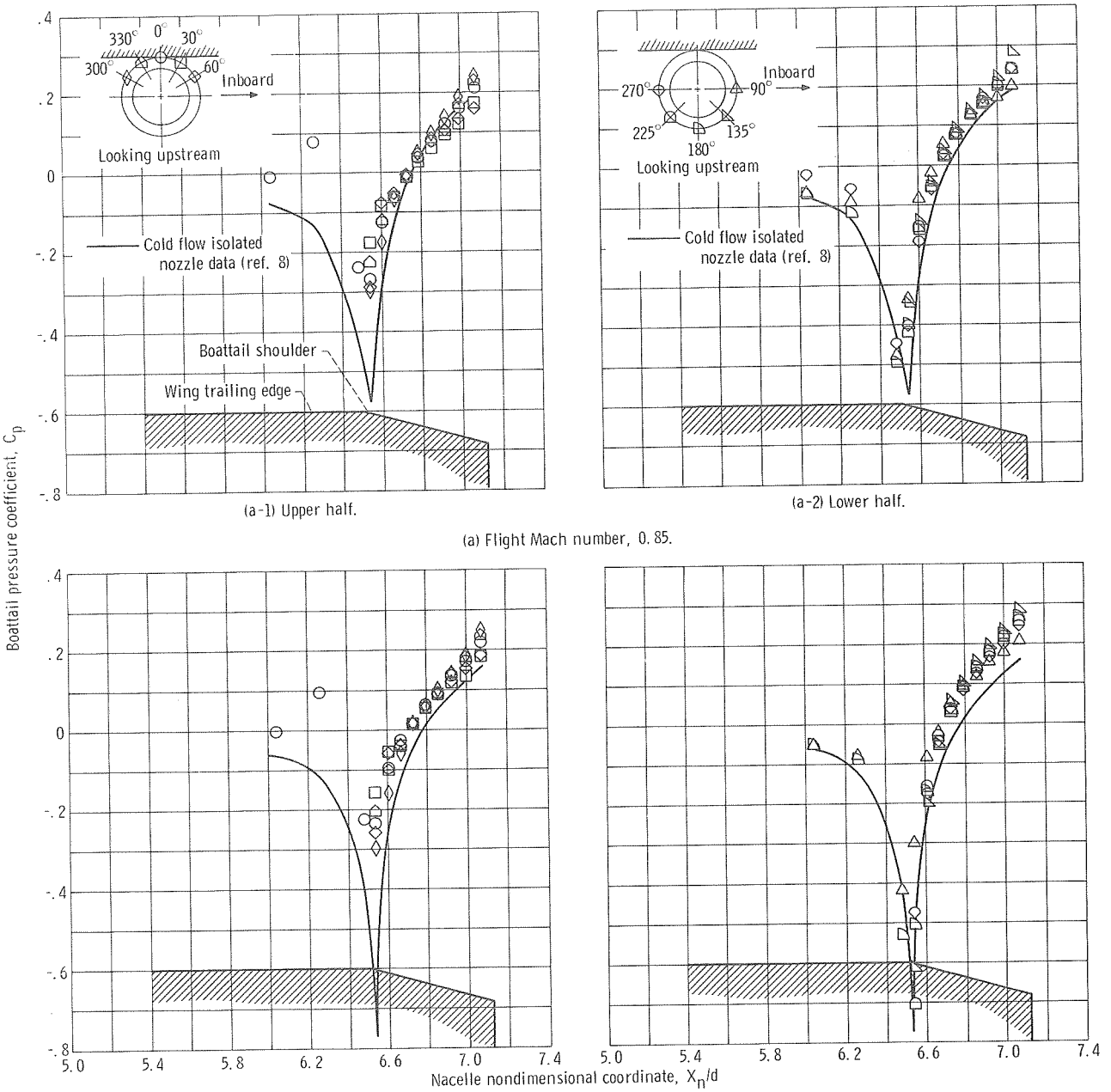

(a-1) Upper half.

(a-2) Lower half.

(a) Flight Mach number, 0.85.

(b-1) Upper half.

(b-2) Lower half.

(b) Flight Mach number, 0.90.

Figure 24. - Comparison of boattail pressure distribution with isolated nozzle data. Radius ratio, 0.5; nozzle exit to primary throat diameter ratio, 1.14.

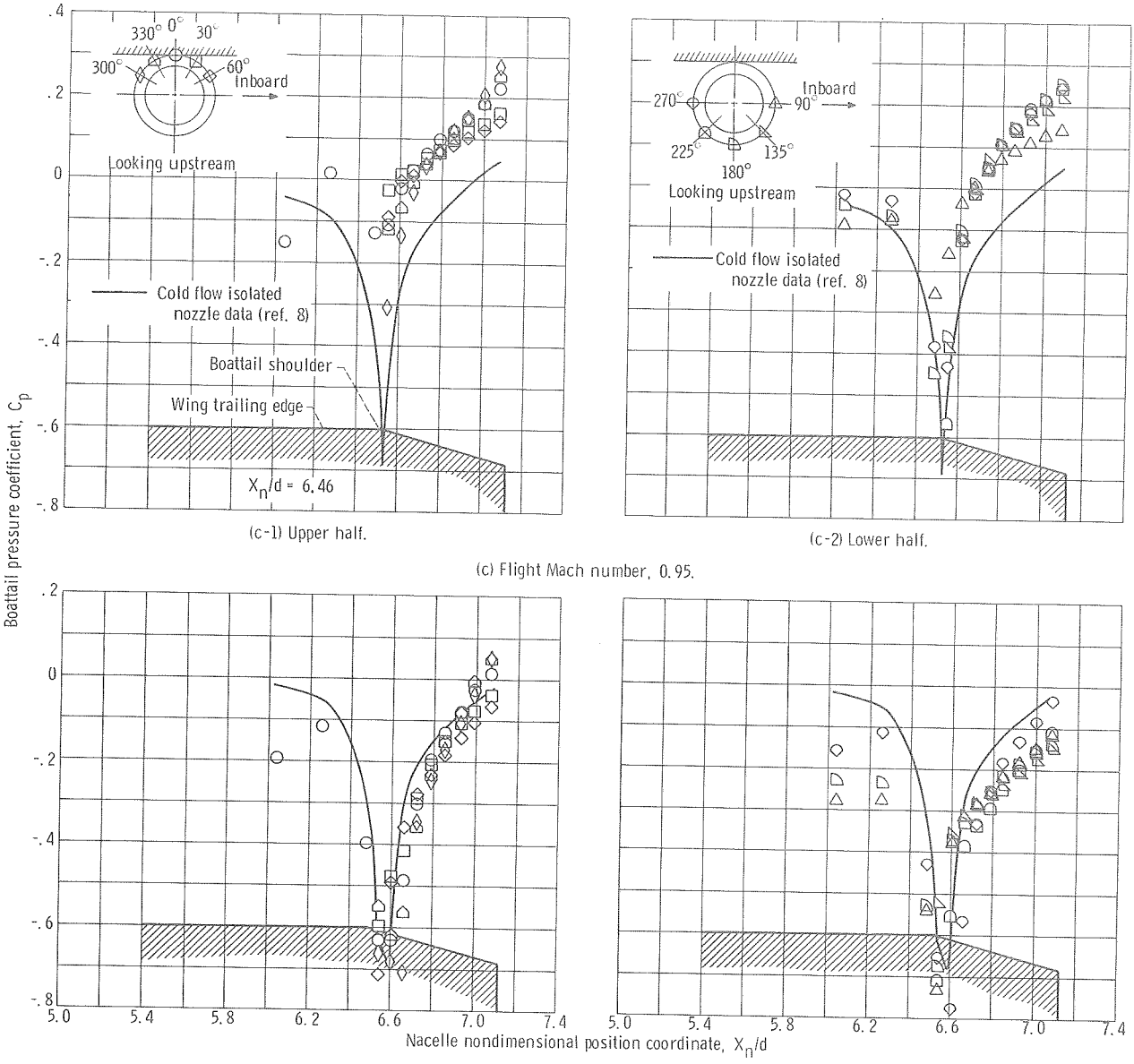

(c-1) Upper half.

(c-2) Lower half.

(c) Flight Mach number, 0.95.

(d-1) Upper half.

(d-2) Lower half.

(d) Flight Mach number, 1.00.

Figure 24. - Continued.

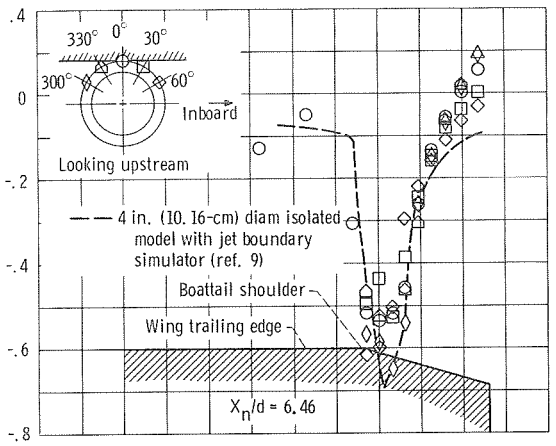

(e-1) Upper half.

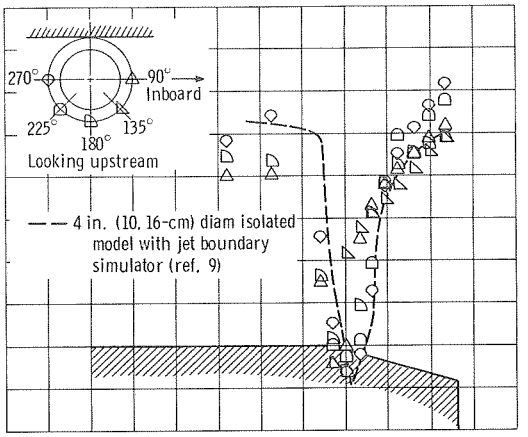

(e-2) Lower half.

(e) Flight Mach number, 1.00.

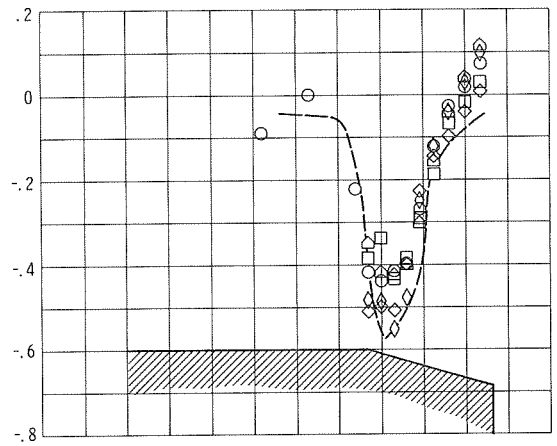

(f-1) Upper half.

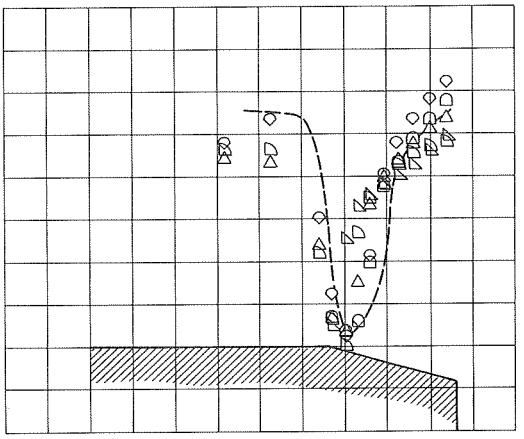

(f-2) Lower half.

(f) Flight Mach number, 1.10.

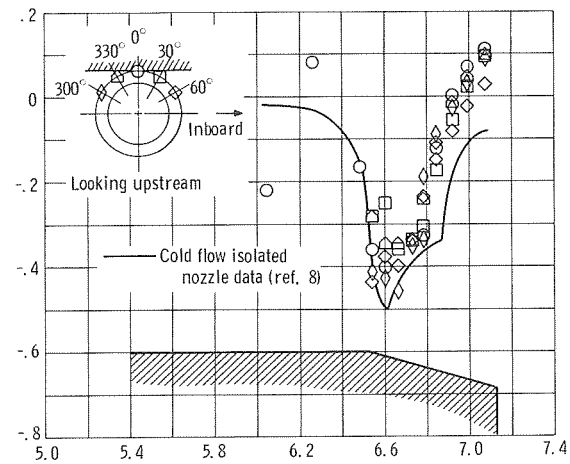

(g-1) Upper half.

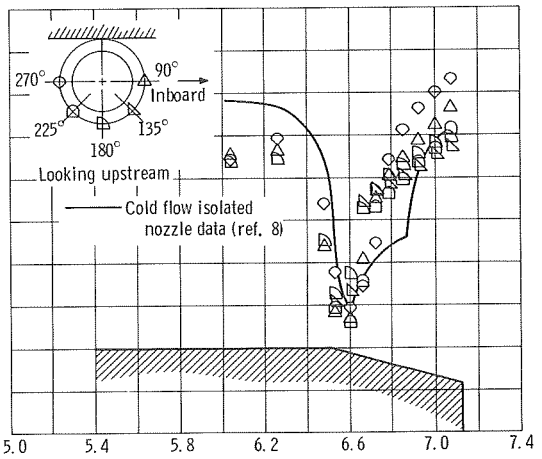

Nacelle nondimensional position coordinate, X_n/d

(g-2) Lower half.

(g) Flight Mach number, 1.20.

Figure 24. - Concluded.

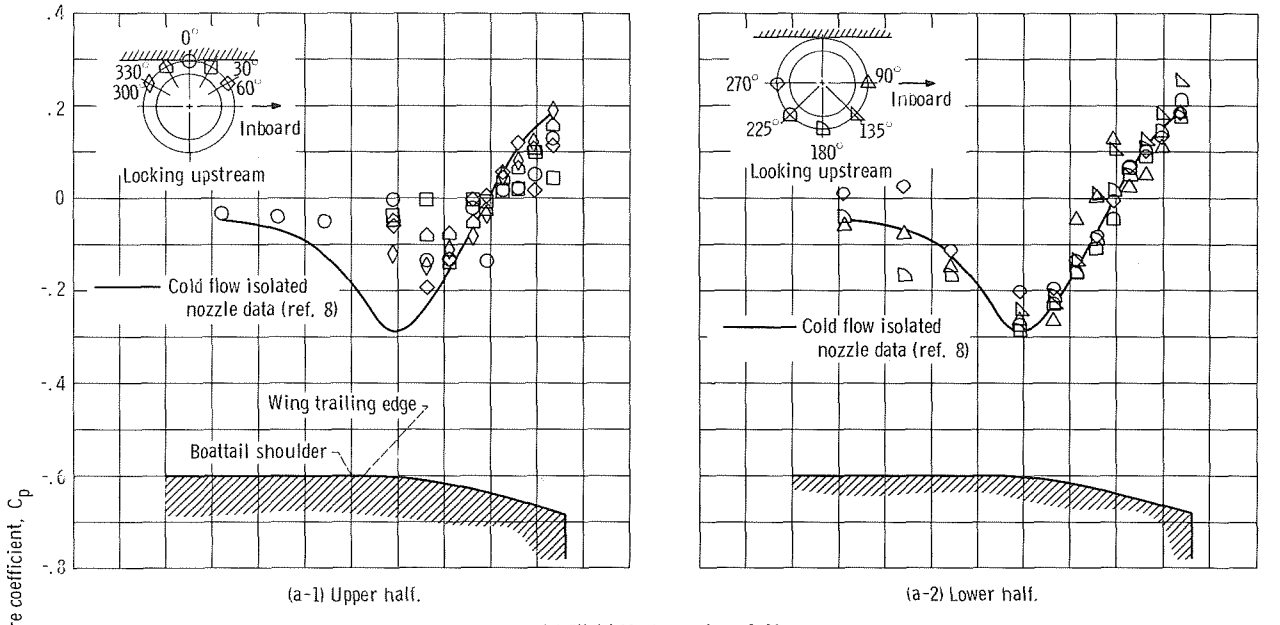

(a-1) Upper half.

(a-2) Lower half.

(a) Flight Mach number, 0.90.

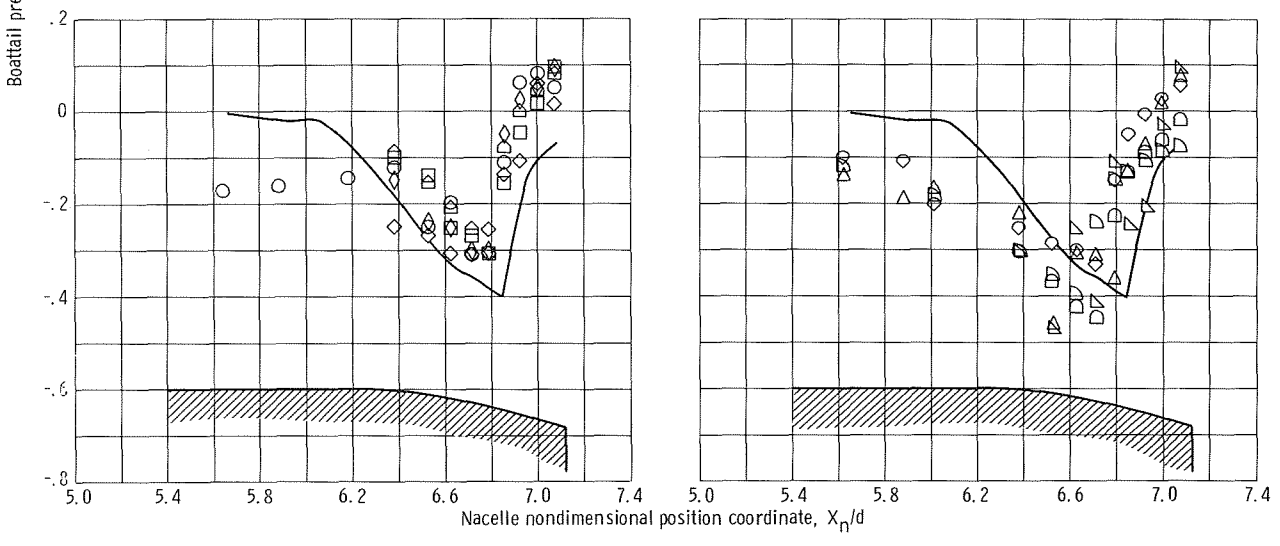

(b-1) Upper half.

(b-2) Lower half.

(b) Flight Mach number, 1.20.

Figure 25. - Comparison of boattail pressure distribution with isolated nozzle data. Radius ratio, 2.5; nozzle exit to primary throat diameter ratio, 1.14.

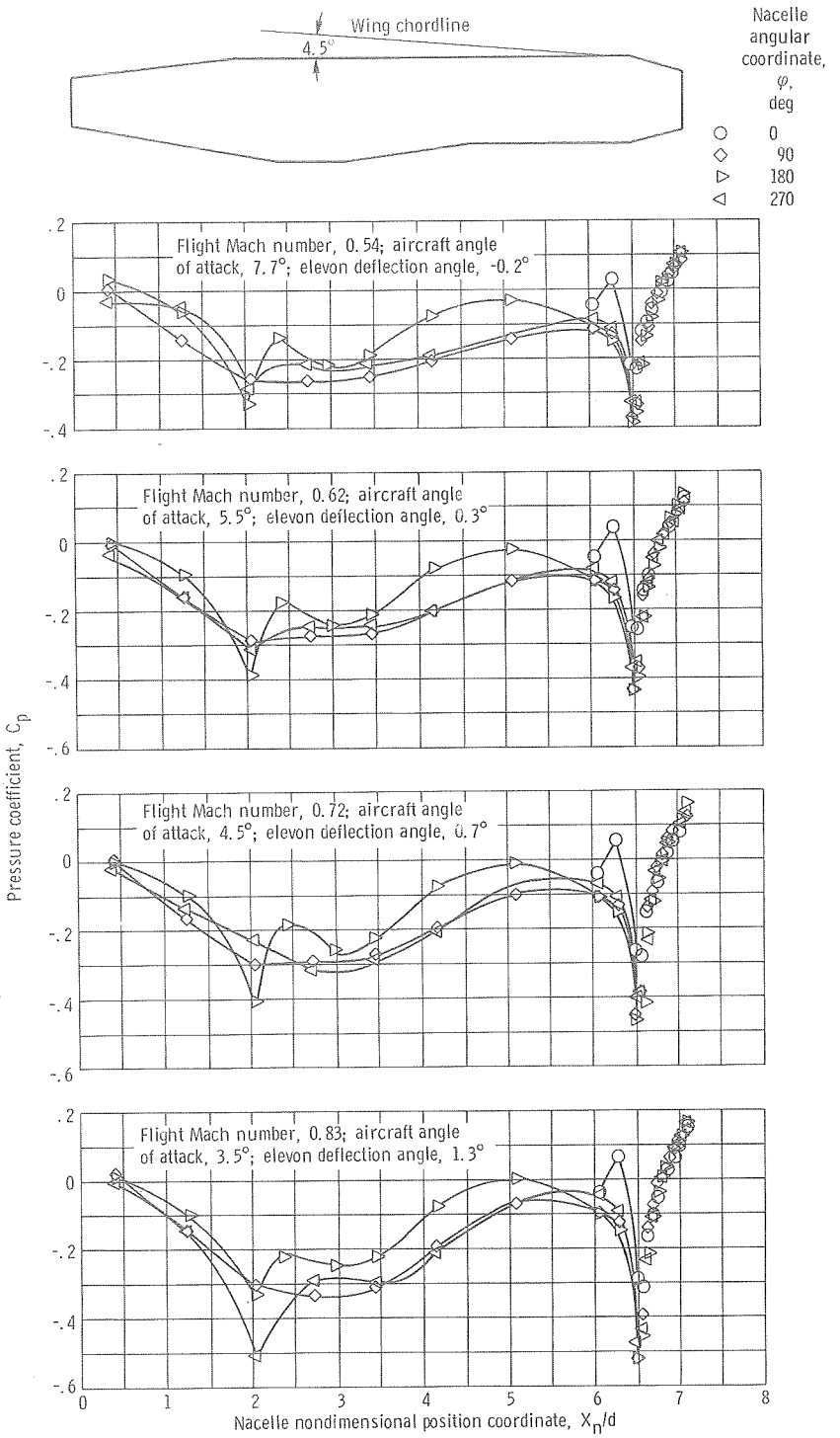

Figure 26. - Nacelle pressure distribution. Radius ratio, 0.5; nozzle exit to primary throat diameter ratio, 1.45.

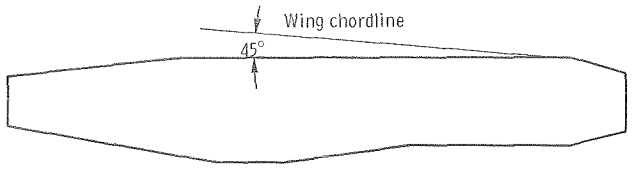

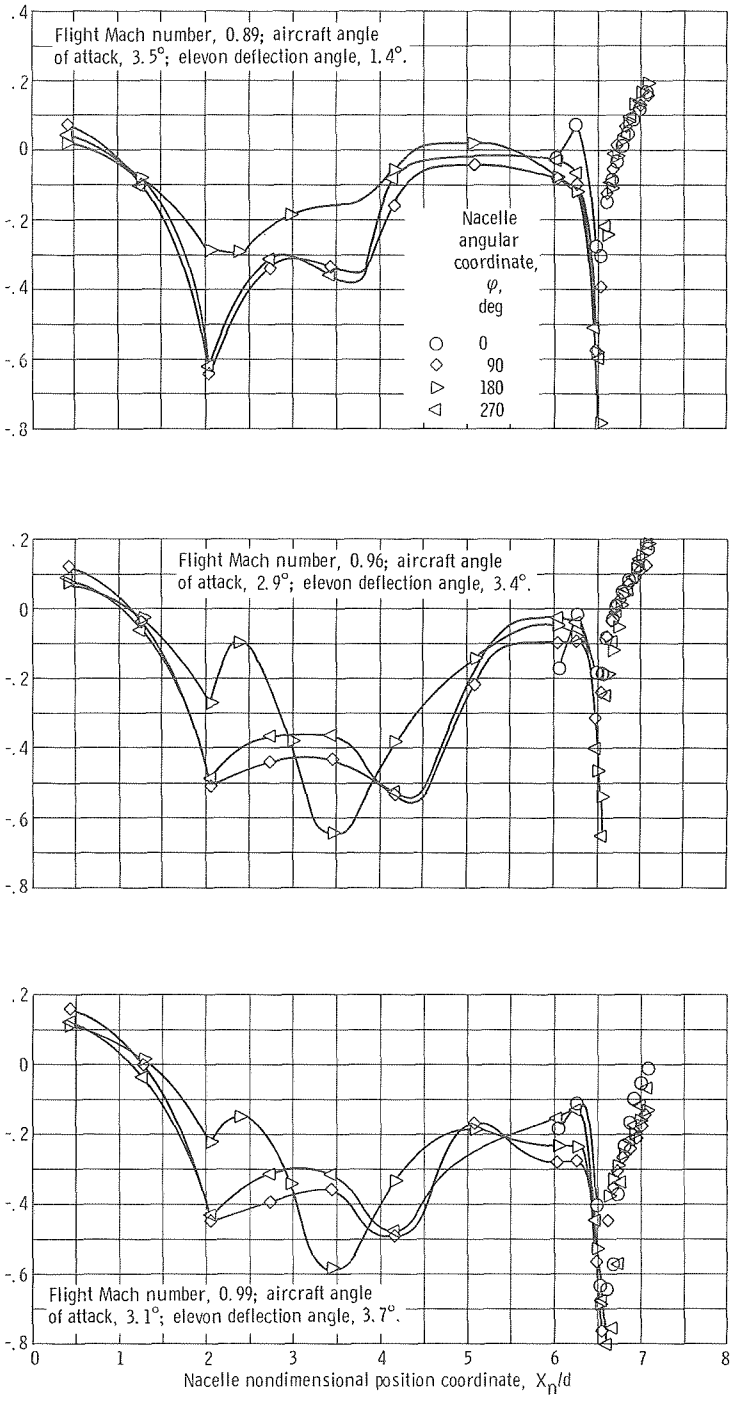

Figure 26. - Continued.

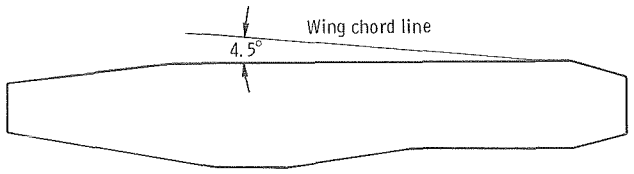

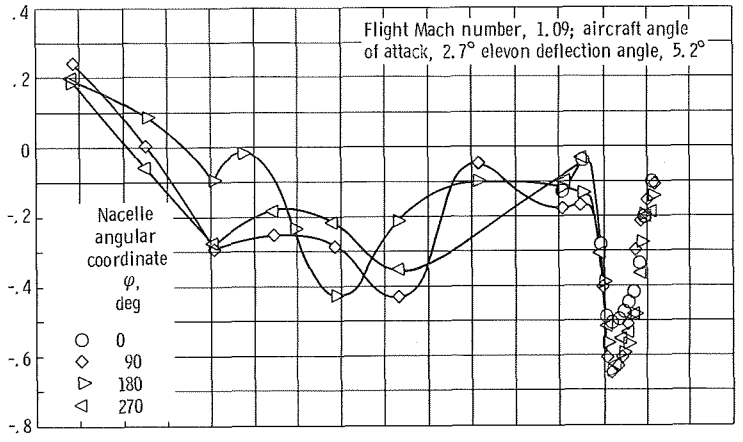

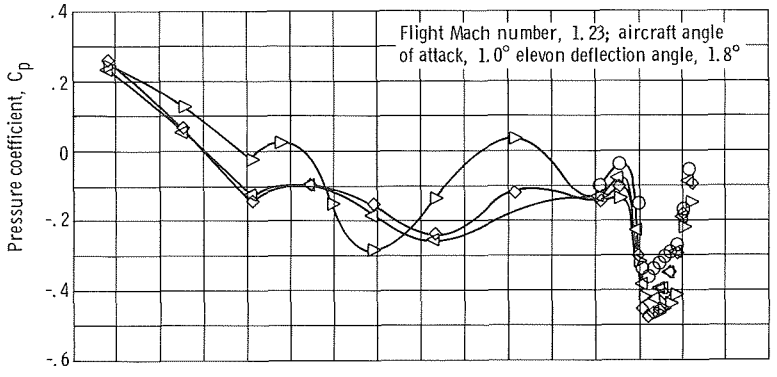

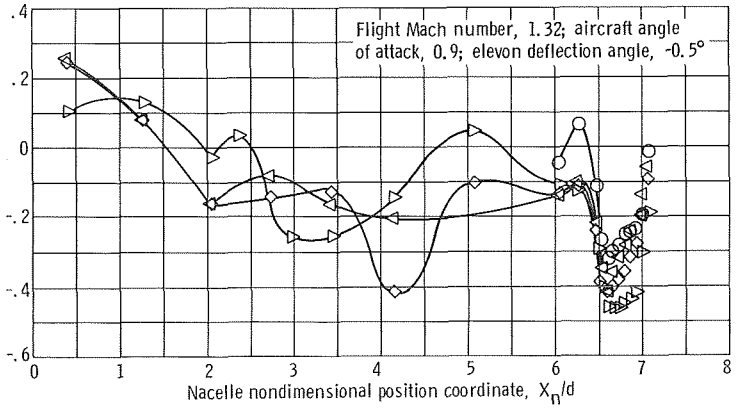

Figure 26. - Concluded.

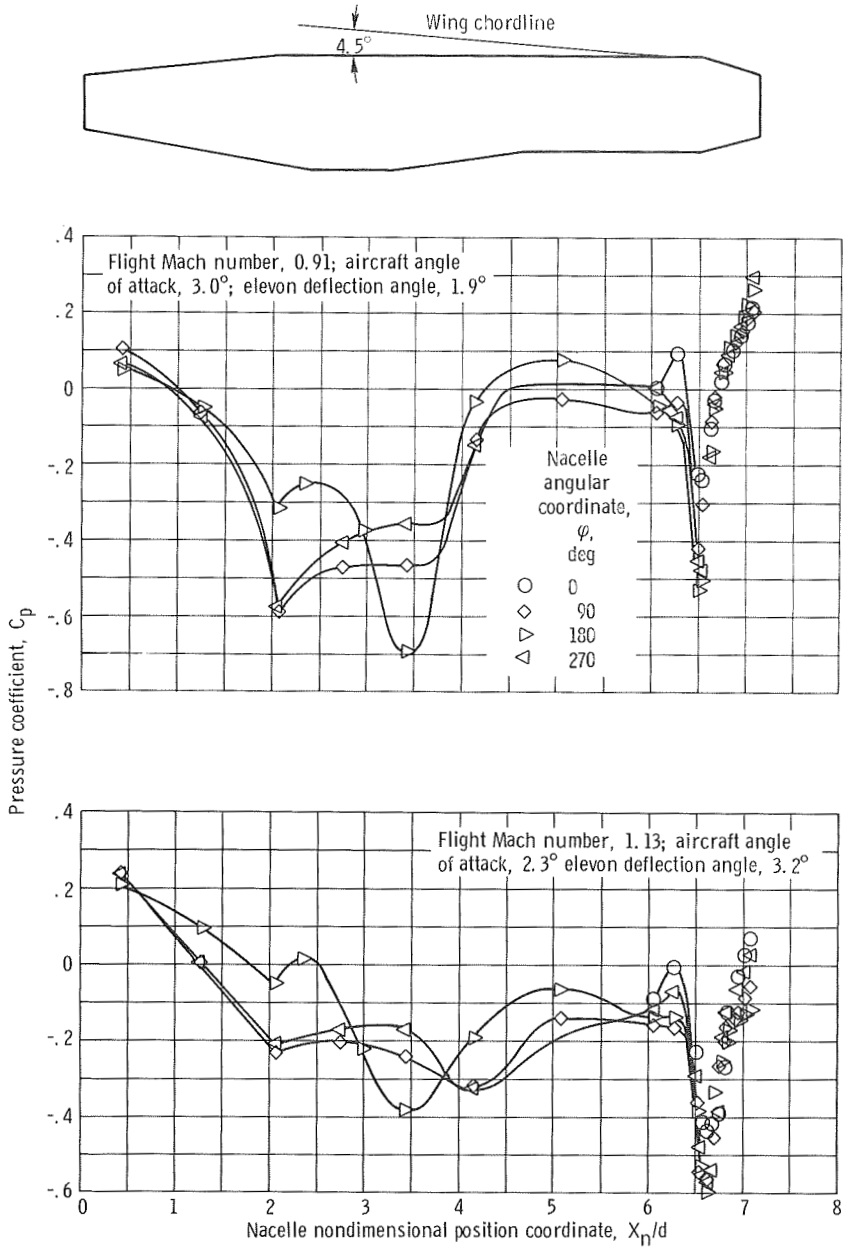

Figure 27. - Nacelle pressure distribution. Radius ratio, 0.5; nozzle exit to primary throat diameter ratio 1.14.

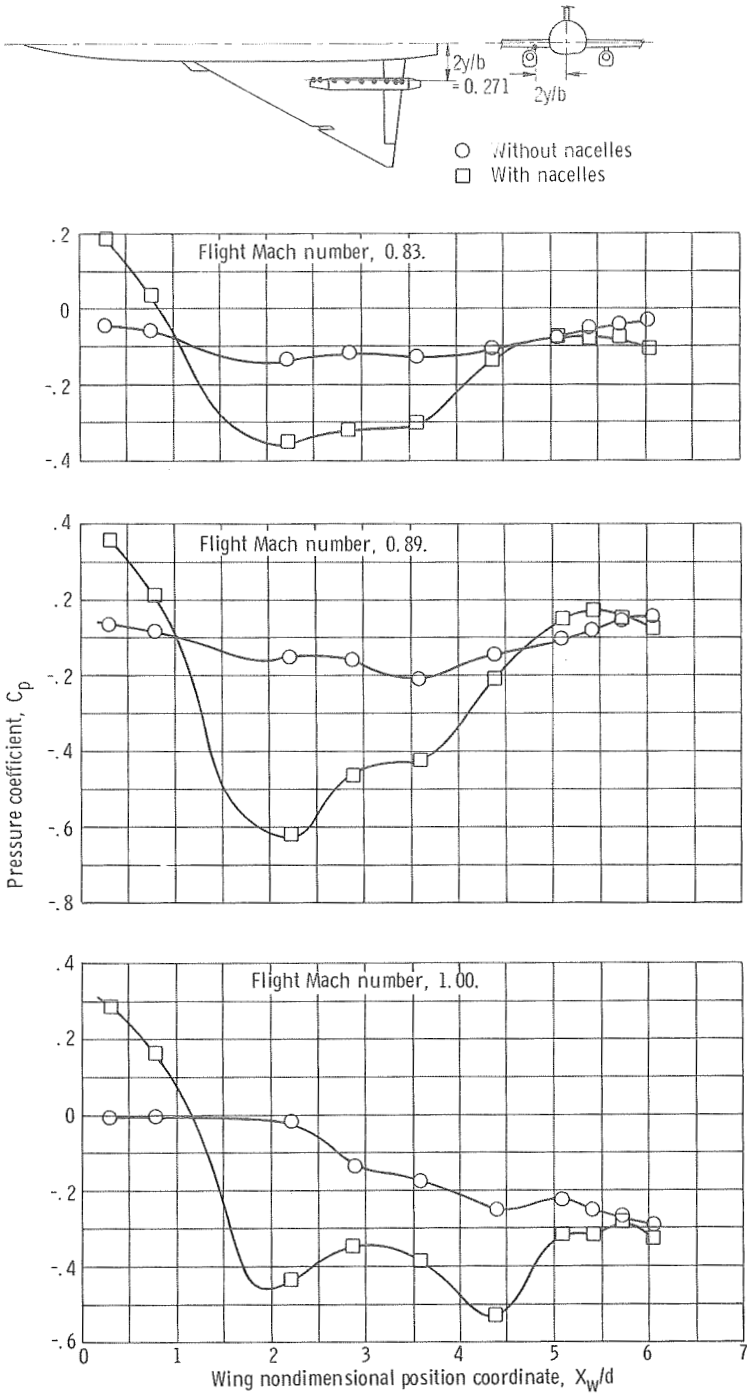

Figure 28. - Effect of nacelle installation on wing lower surface pressure distribution.

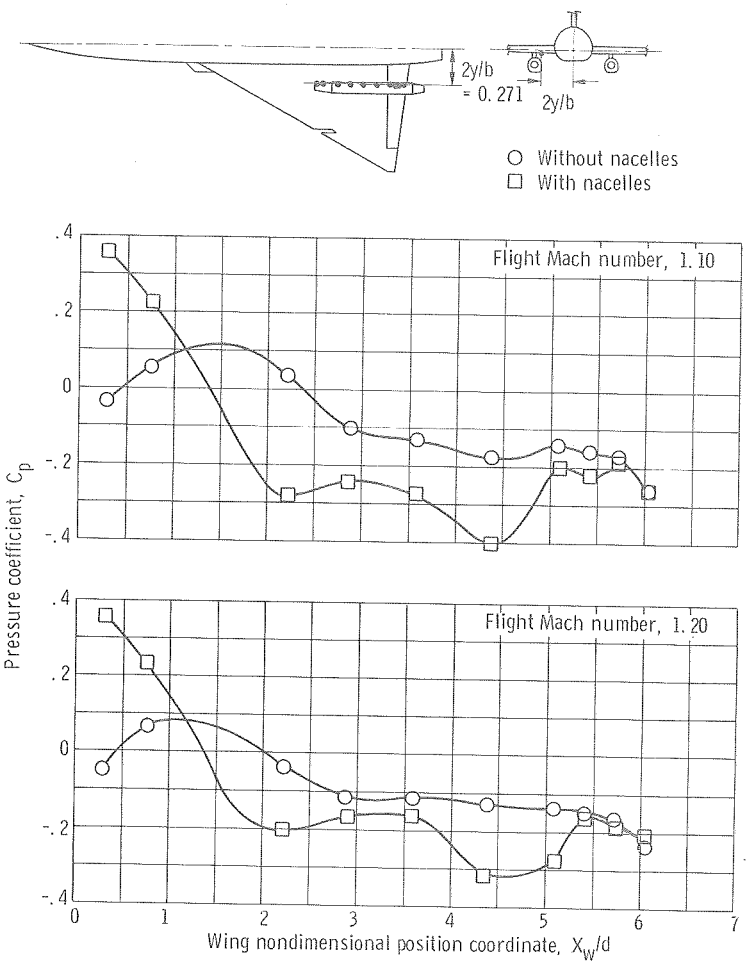

Figure 28. - Concluded.

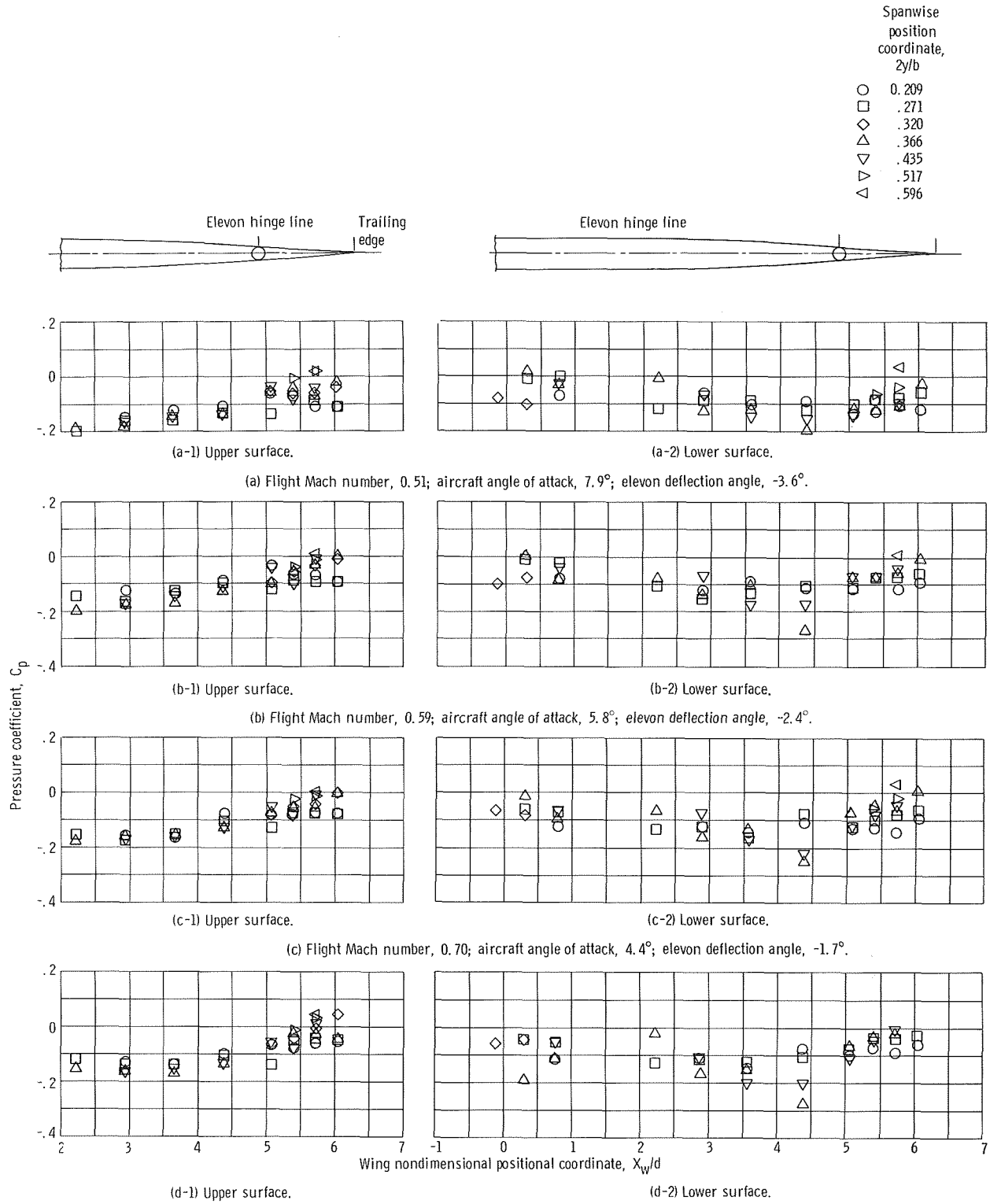

(a-1) Upper surface.

(a-2) Lower surface.

(a) Flight Mach number, 0.51; aircraft angle of attack, 7.9°; elevon deflection angle, -3.6°.

(b-1) Upper surface.

(b-2) Lower surface.

(b) Flight Mach number, 0.59; aircraft angle of attack, 5.8°; elevon deflection angle, -2.4°.

(c-1) Upper surface.

(c-2) Lower surface.

(c) Flight Mach number, 0.70; aircraft angle of attack, 4.4°; elevon deflection angle, -1.7°.

(d-1) Upper surface.

(d-2) Lower surface.

(d) Flight Mach number, 0.83; aircraft angle of attack, 3.3°; elevon deflection angle, -1.1°.

Figure 29. - Wing pressure distribution without nacelles installed.

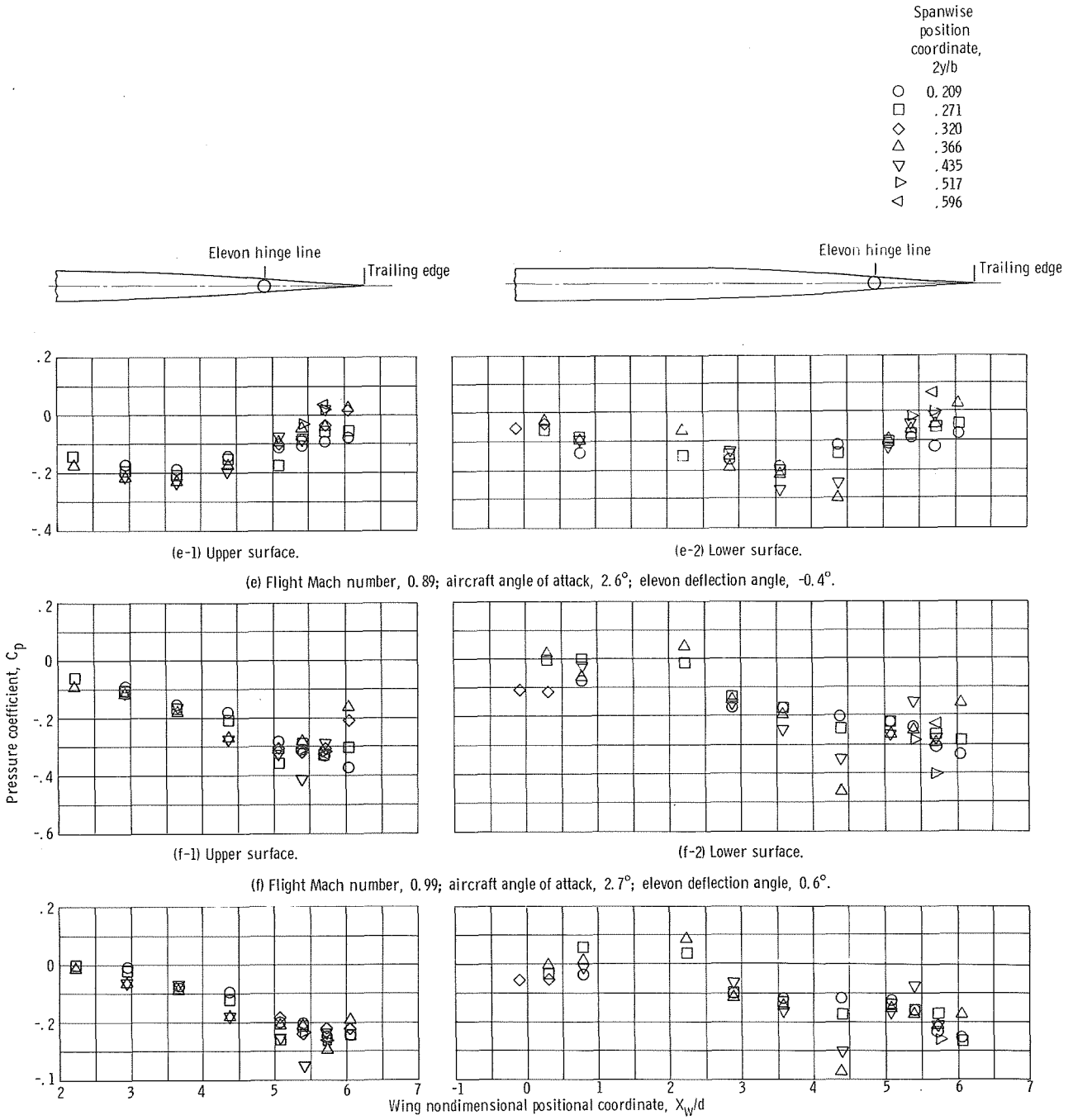

Figure 29. - Continued.

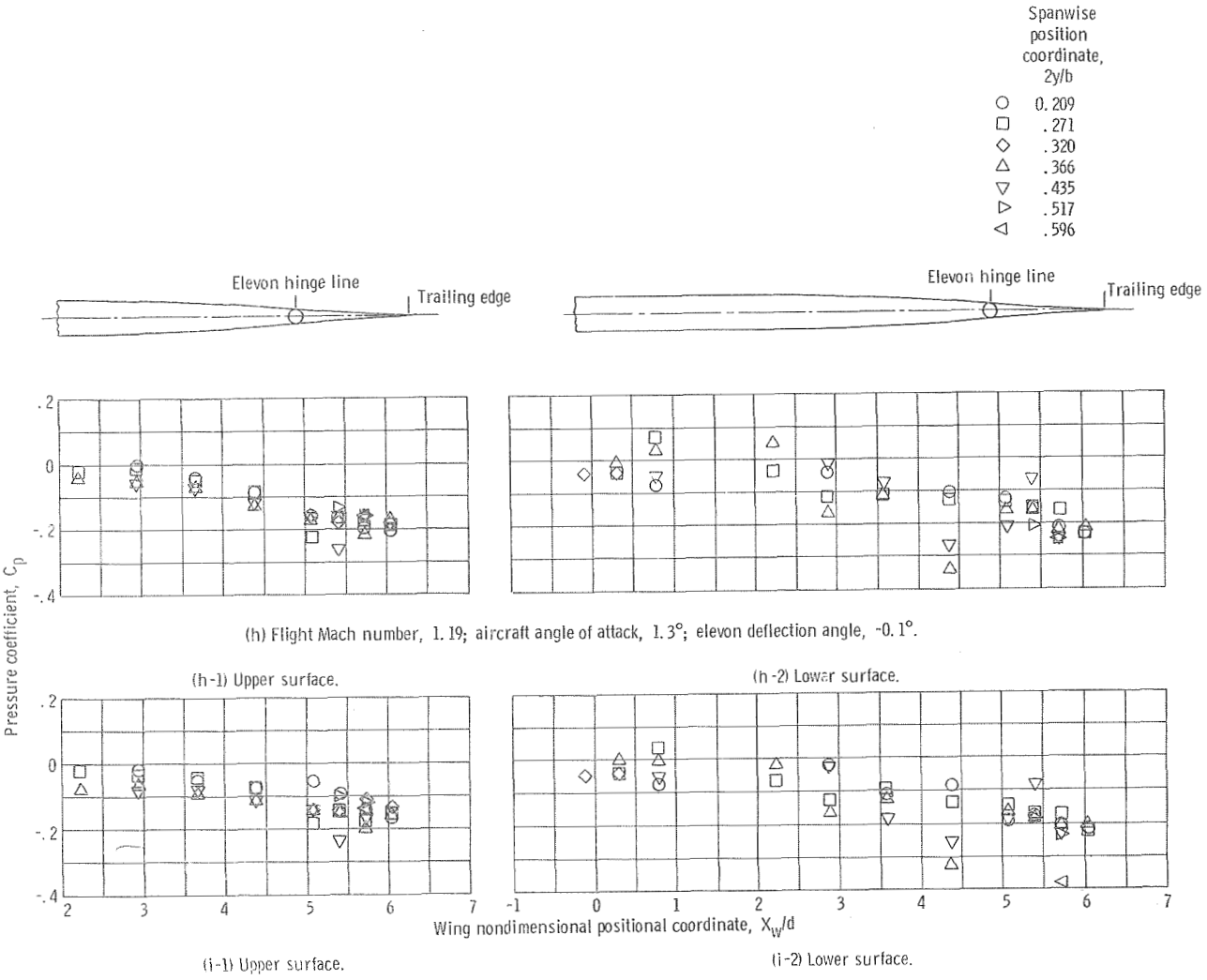

(h) Flight Mach number, 1.19; aircraft angle of attack, 1.3°; elevon deflection angle, -0.1°.

(i) Flight Mach number, 1.29; aircraft angle of attack, 0.7°; elevon deflection angle, -1.4.

Figure 29. - Concluded.

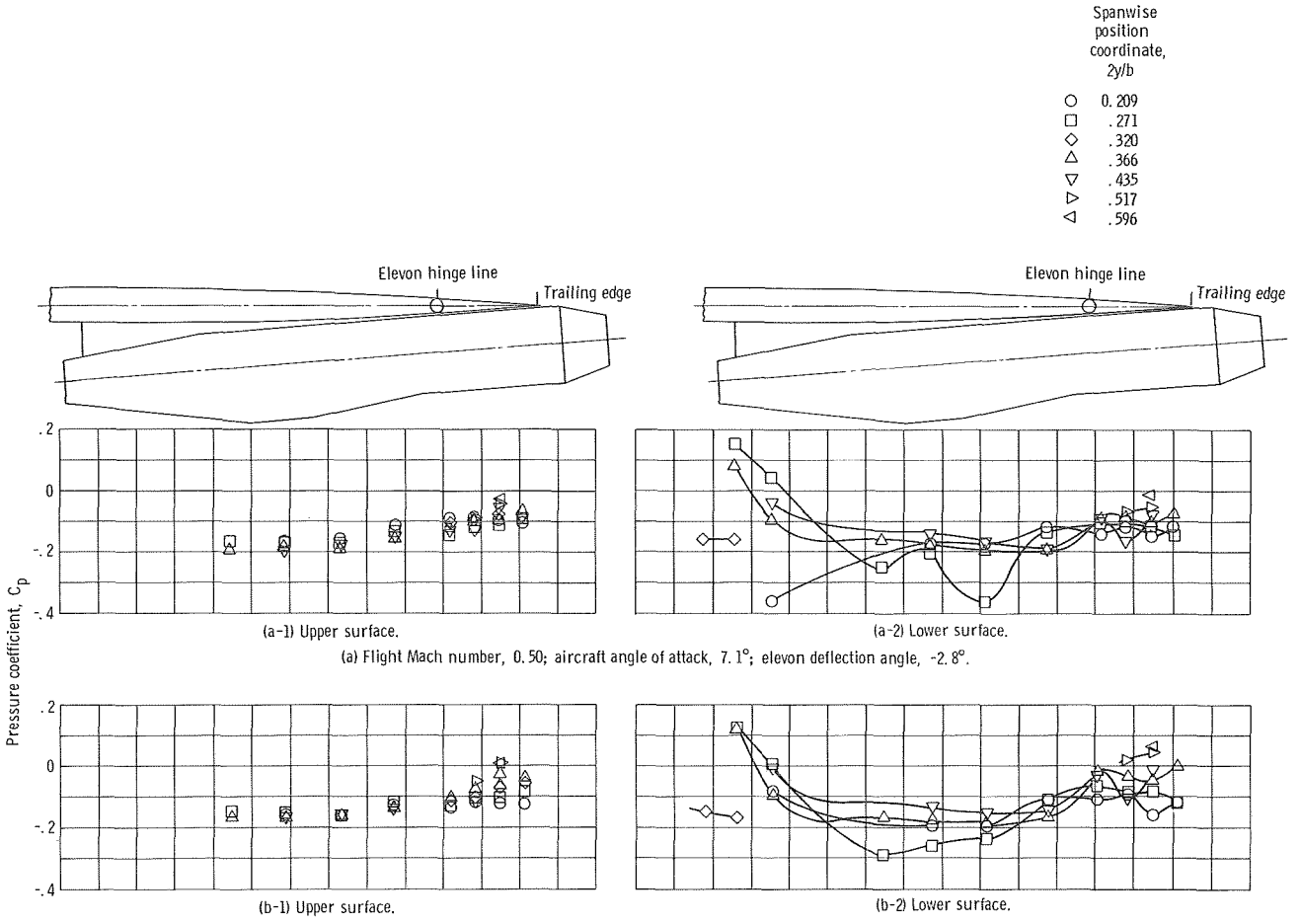

(a) Flight Mach number, 0.50; aircraft angle of attack, 7.1°; elevon deflection angle, -2.8°.

(b) Flight Mach number, 0.60; aircraft angle of attack, 4.6°; elevon deflection angle, 0.1°.

Figure 30. - Wing pressure distribution with nacelles installed.

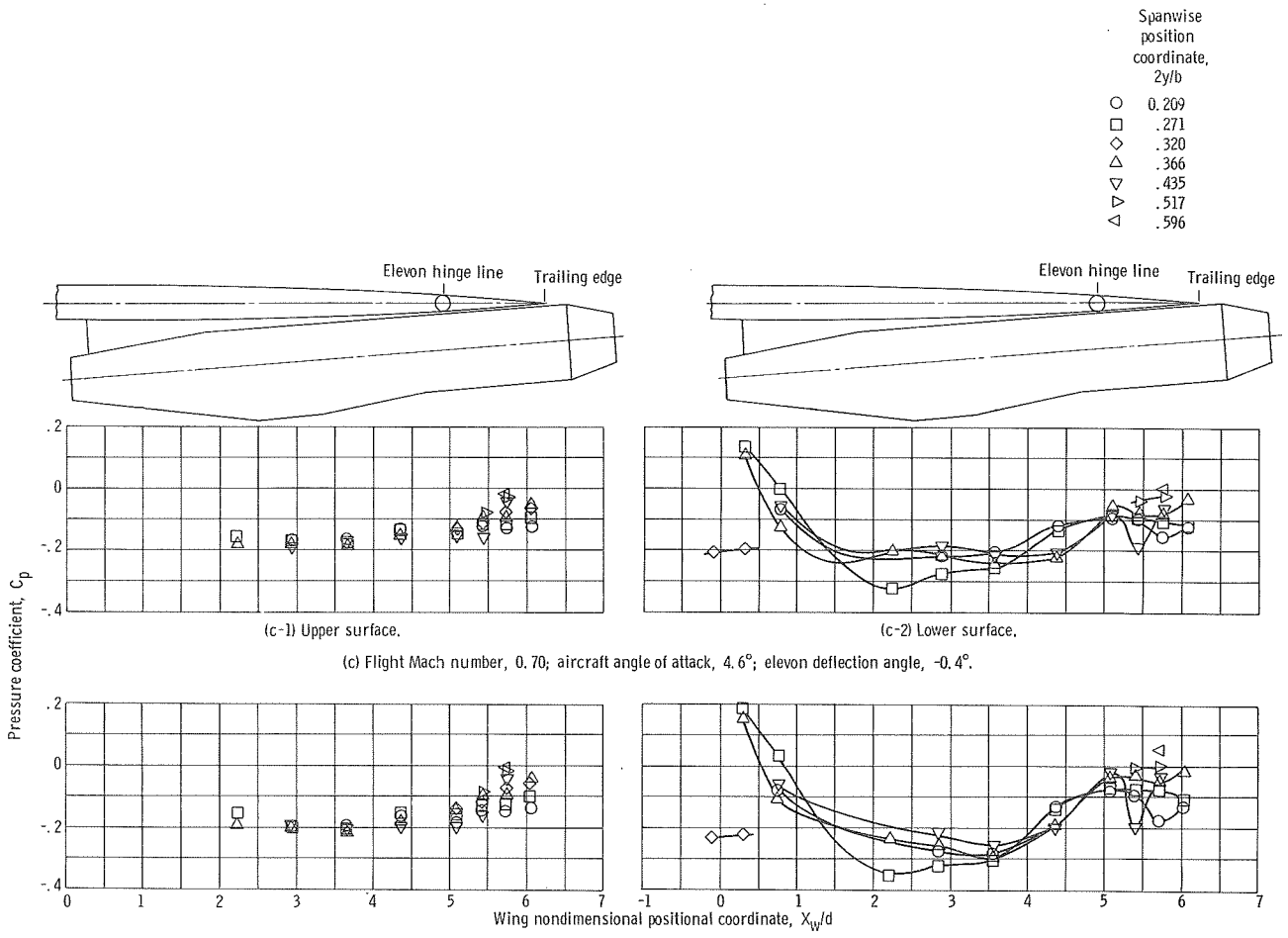

(c-1) Upper surface.

(c-2) Lower surface.

(c) Flight Mach number, 0.70; aircraft angle of attack, 4.6°; elevon deflection angle, -0.4°.

(d-1) Upper surface.

(d-2) Lower surface.

(d) Flight Mach number, 0.82; aircraft angle of attack, 3.6°; elevon deflection angle, 0.2°.

Figure 30. - Continued.

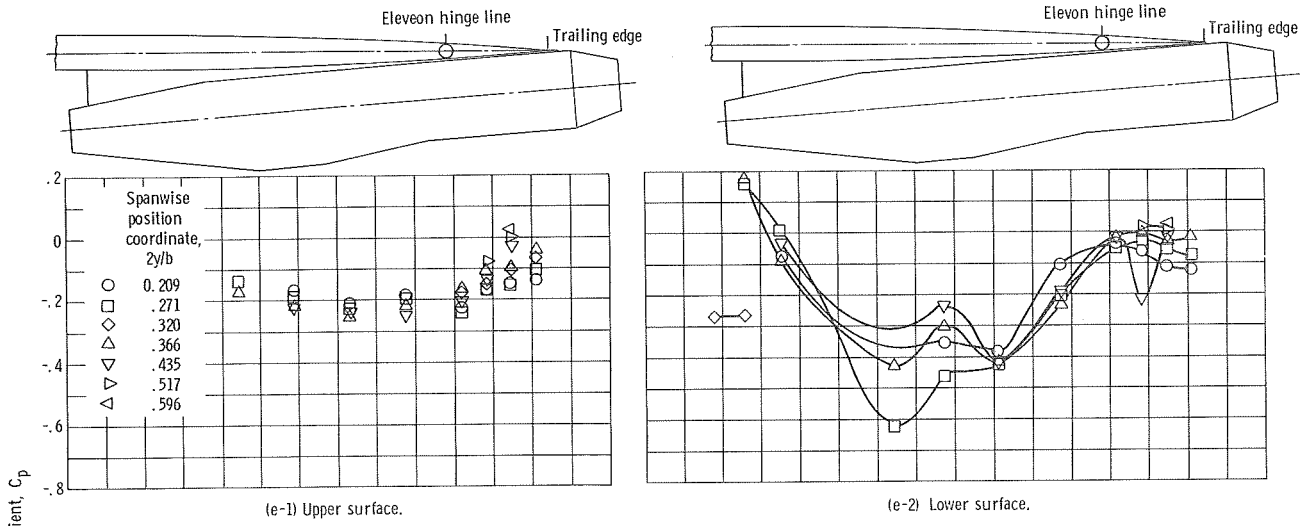

(e-1) Upper surface.

(e-2) Lower surface.

(e) Flight Mach number, 0.89; aircraft angle of attack, 2.9°; elevon deflection angle, 1.2°.

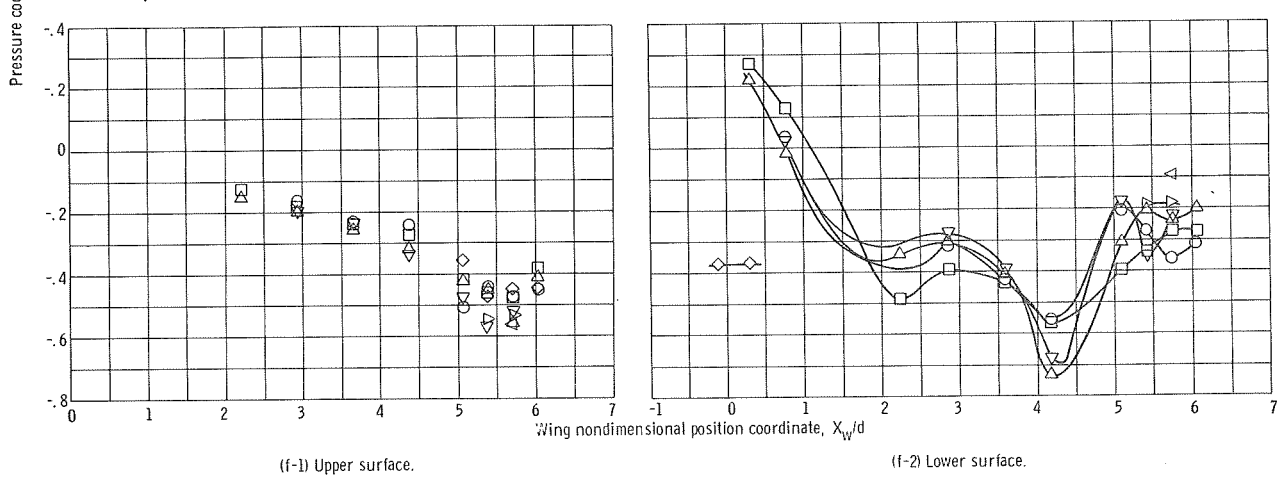

(f-1) Upper surface.

(f-2) Lower surface.

(f) Flight Mach number, 0.97; aircraft angle of attack, 3.2°; elevon deflection angle, 1.8°.

Figure 30. - Continued.

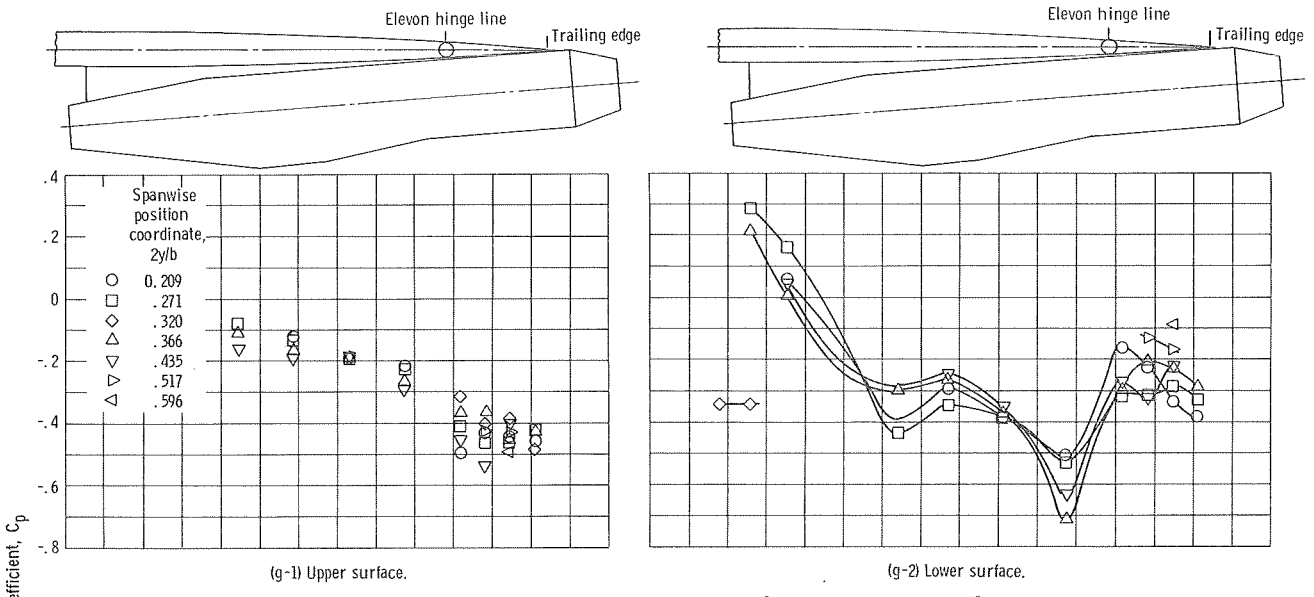

(g-1) Upper surface.

(g-2) Lower surface.

(g) Flight Mach number, 1.00; aircraft angle of attack, 3.2°; elevon deflection angle, 1.3°.

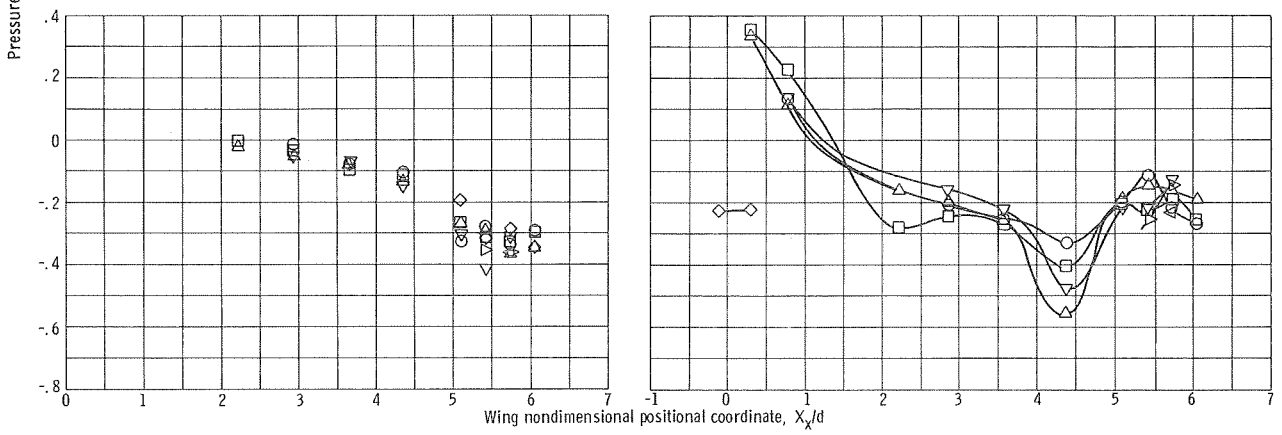

(h-1) Upper surface.

(h-2) Lower surface.

(h) Flight Mach number, 1.12; angle of attack, 2.5°; elevon deflection angle, 2.4°.

Figure 30. - Continued.

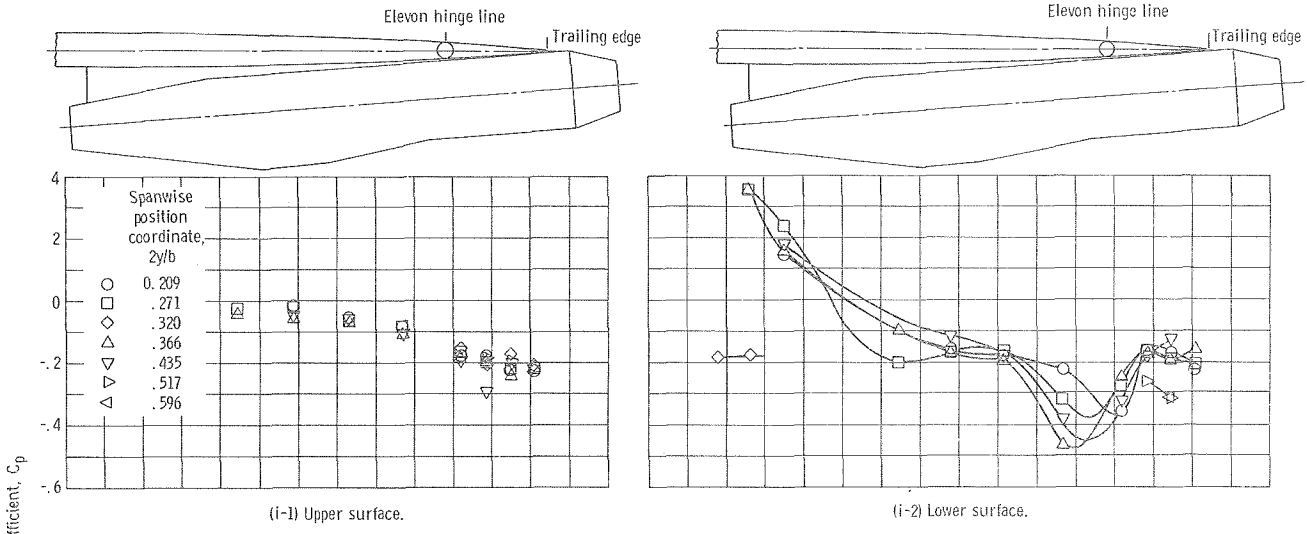

(i-1) Upper surface.

(i-2) Lower surface.

(i) Flight Mach number, 1.21; aircraft angle of attack, 1.2°; elevon deflection angle, -0.4°.

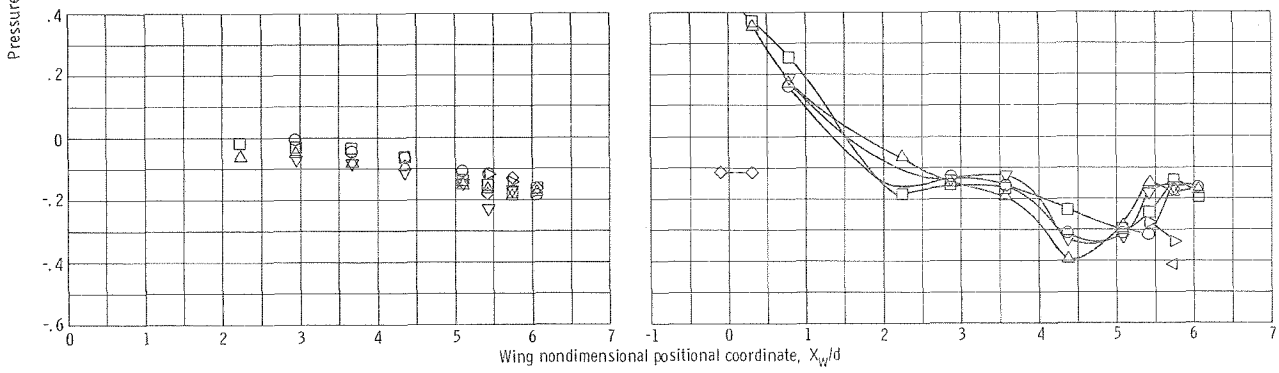

(j-1) Upper surface.

(j-1) Upper surface.

(j) Flight Mach number, 1.29; aircraft angle of attack, 0.9°; elevon deflection angle, 1.9°.

Figure 30. - Concluded.

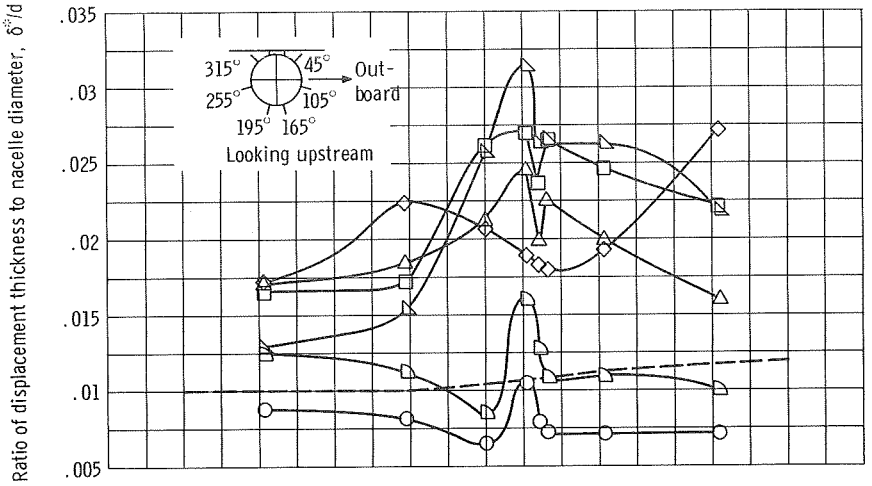

(a) Displacement thickness.

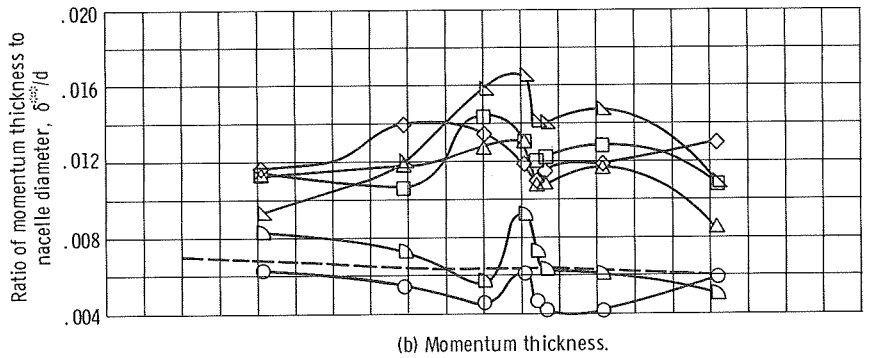

(b) Momentum thickness.

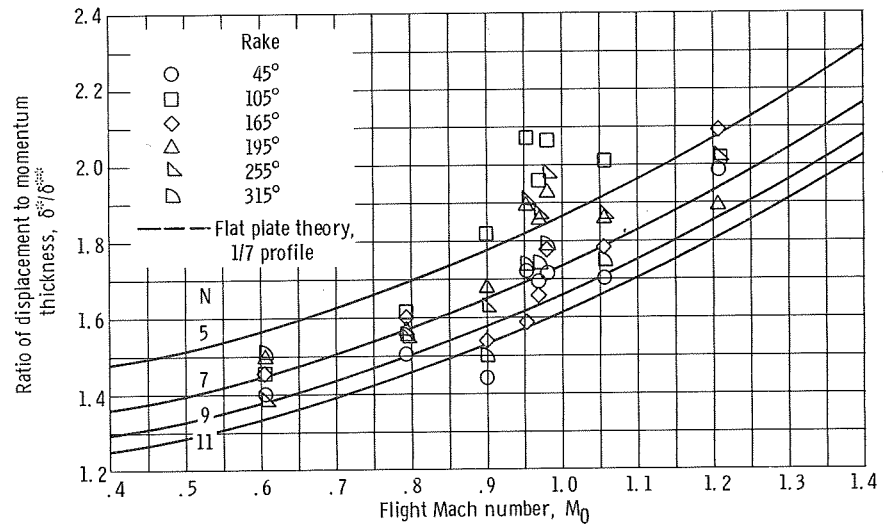

(c) Ratio of displacement to momentum thickness showing exponent in boundary-layer velocity equation $V/V_{bl} = (z/\delta)^{1/N}$.

Figure 31. - Nacelle boundary-layer characteristics.

Rake	Ratio of momentum thickness to nacelle diameter, δ^{**}/d	Boundary layer to free-stream velocity ratio, V_{bl}/V_0	Boundary layer to free-stream total pressure ratio, P_{bl}/P_0
○ 45°	0.006	0.965	0.967
□ 105°	.011	.993	.980
◇ 165°	.012	.989	.980
△ 195°	.0113	.997	.983
◺ 255°	.009	1.006	.981
◺ 315°	.008	.983	.970

Flight Mach number, 0.61; inlet capture mass flow ratio, 0.91

Rake	δ^{**}/d	V_{bl}/V_0	P_{bl}/P_0
○ 45°	0.005	0.871	0.878
□ 105°	.014	.984	.983
◇ 165°	.014	.951	.949
△ 195°	.013	.986	.982
◺ 255°	.016	.940	.913
◺ 315°	.006	.738	.773

Flight Mach number, 0.90; inlet capture mass flow ratio, 0.78

Rake	δ^{**}/d	V_{bl}/V_0	P_{bl}/P_0
○ 45°	0.006	0.957	0.958
□ 105°	.011	.999	.982
◇ 165°	.014	.986	.969
△ 195°	.012	.979	.966
◺ 255°	.010	1.012	.983
◺ 315°	.007	.964	.947

Flight Mach number, 0.79; inlet capture mass flow ratio, 0.81

Rake	δ^{**}/d	V_{bl}/V_0	P_{bl}/P_0
○ 45°	0.006	0.940	0.899
□ 105°	.013	1.008	.977
◇ 165°	.012	.974	.932
△ 195°	.013	1.027	.980
◺ 255°	.017	1.037	.964
◺ 315°	.009	.835	.764

Flight Mach number, 0.95; inlet capture mass flow ratio, 0.78

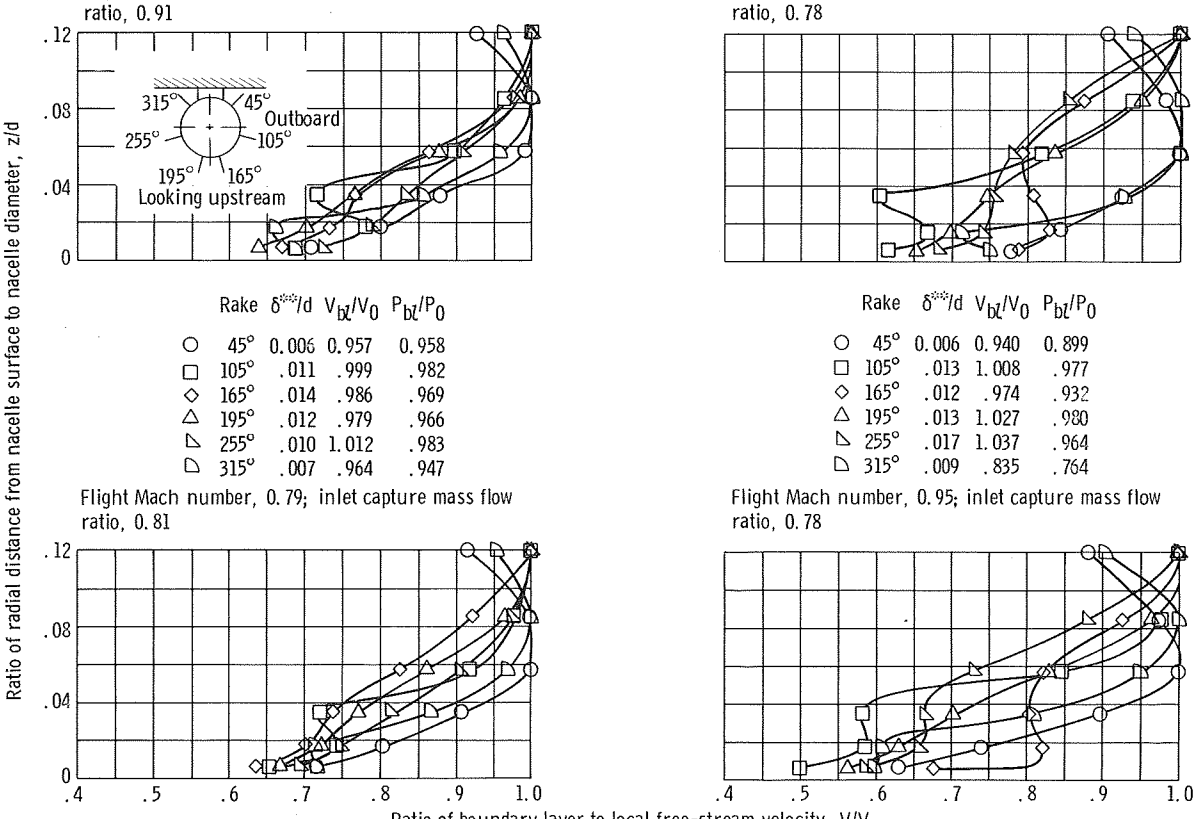

Figure 32. - Nacelle boundary-layer velocity profiles.

	Rake	Ratio of momentum thickness to nacelle diameter, δ^{**}/d	Boundary layer to free-stream velocity ratio, $V_{b\ell}/V_0$	Boundary layer to free-stream total pressure ratio, $P_{b\ell}/P_0$
○	45°	0.004	1.011	0.916
□	105°	.012	1.055	.964
◇	165°	.012	1.035	.913
△	195°	.011	1.080	.971
▷	255°	.014	1.079	.955
⬠	315°	.006	.985	.849

Flight Mach number, 0.98; inlet capture mass flow ratio, 0.77

	Rake	δ^{**}/d	$V_{b\ell}/V_0$	$P_{b\ell}/P_0$
○	45°	0.004	0.967	0.912
□	105°	.013	1.015	.963
◇	165°	.012	.996	.896
△	195°	.012	1.040	.969
▷	255°	.015	1.035	.957
⬠	315°	.006	.960	.858

Flight Mach number, 1.06; inlet capture mass flow ratio, 0.76

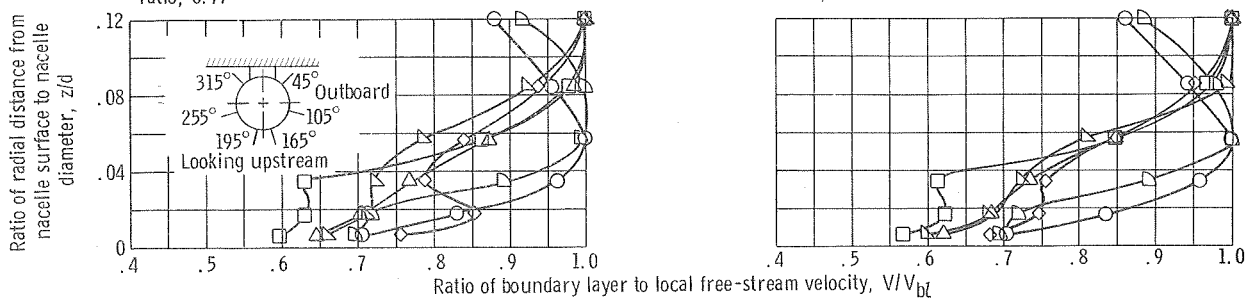

	Rake	δ^{**}/d	$V_{b\ell}/V_0$	$P_{b\ell}/P_0$
○	45°	0.005	1.025	0.953
□	105°	.011	1.039	.974
◇	165°	.013	1.024	.978
△	195°	.009	1.010	.957
▷	255°	.011	1.045	.957
⬠	315°	.005	1.050	.938

Flight Mach number, 1.21; inlet capture mass flow ratio, 0.83

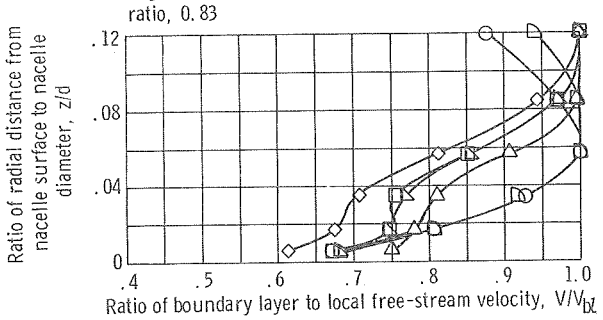

Figure 32. - Concluded.

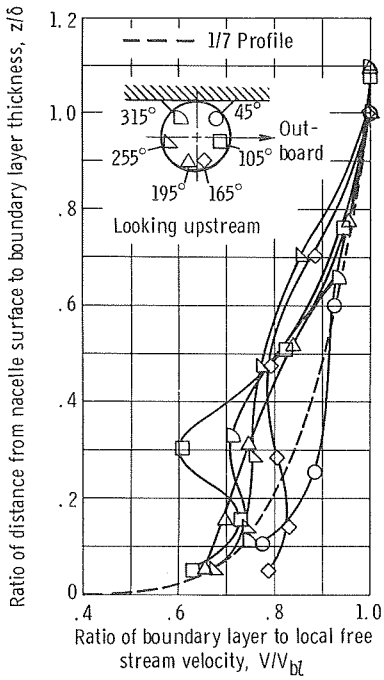

Figure 33. - Typical nacelle boundary-layer velocity profiles. Flight Mach number, 0.90.

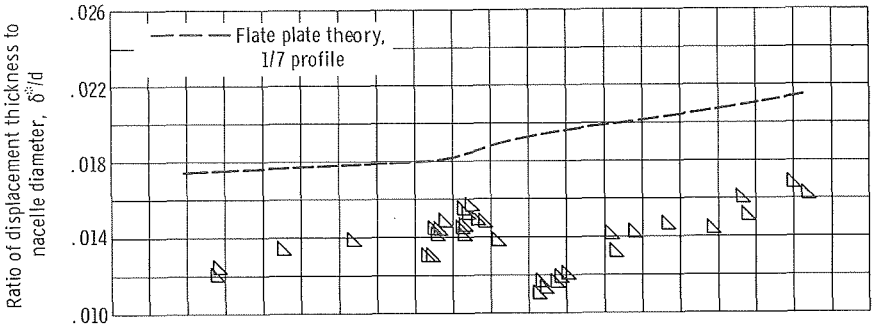

(a) Displacement thickness.

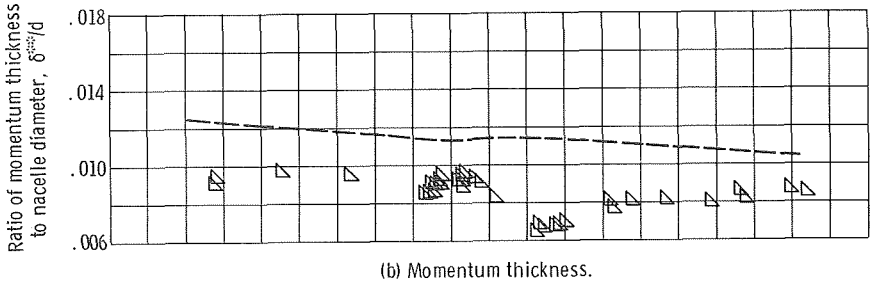

(b) Momentum thickness.

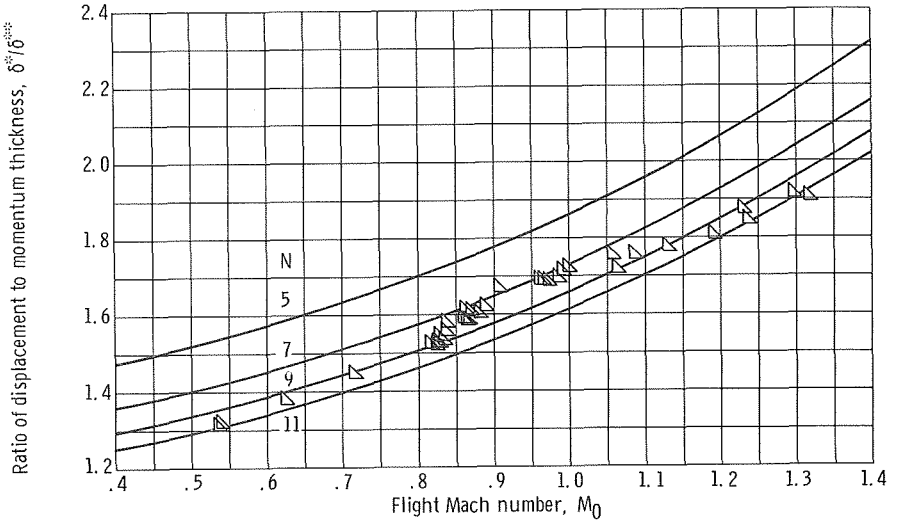

(c) Ratio of displacement to momentum thickness showing exponent in boundary-layer velocity equation $V/V_{bl} = (z/\delta)^{1/N}$.

Figure 34. - Wing boundary-layer characteristics.

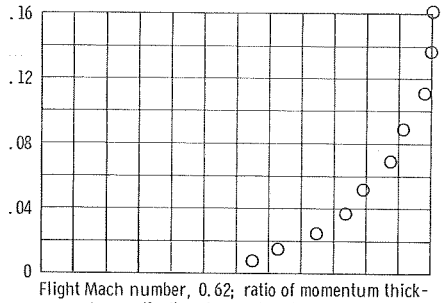

Flight Mach number, 0.62; ratio of momentum thickness to nacelle diameter, 0.010; boundary-layer to free-stream velocity ratio, 1.05; boundary-layer to free-stream total pressure ratio, 0.990.

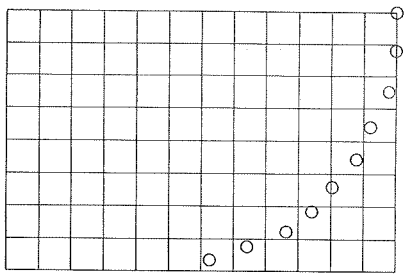

Flight Mach number, 0.83; ratio of momentum thickness to nacelle diameter, 0.009; boundary-layer to free-stream velocity ratio, 1.075; boundary-layer to free-stream total pressure ratio, 0.992.

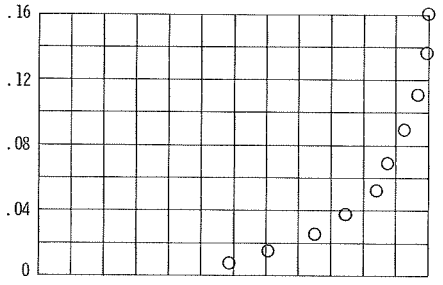

Flight Mach number, 0.88; ratio of momentum thickness to nacelle diameter, 0.009; boundary-layer to free-stream velocity ratio, 1.080; boundary-layer to free-stream total pressure ratio, 0.990.

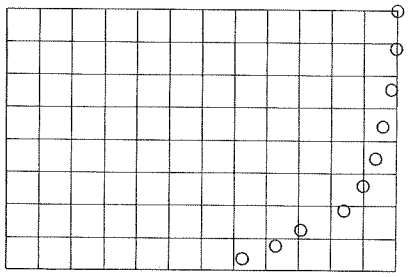

Flight Mach number, 0.96; ratio of momentum thickness to nacelle diameter, 0.007; boundary-layer to free-stream velocity ratio, 1.143; boundary-layer to free-stream total pressure ratio, 0.965.

Ratio of distance from wing surface to nacelle diameter, z/d

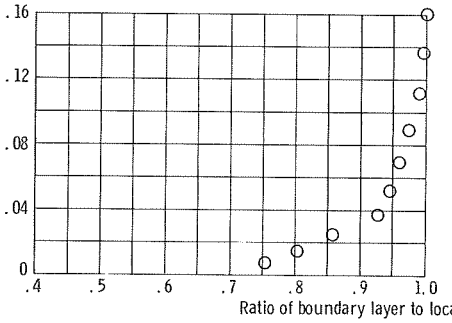

Flight Mach number, 1.00; ratio of momentum thickness to nacelle diameter, 0.007; boundary-layer to free-stream velocity ratio, 1.119; boundary-layer to free-stream total pressure ratio, 0.963.

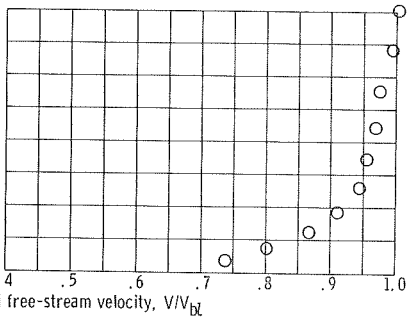

Ratio of boundary layer to local free-stream velocity, V/V_{bl}

Flight Mach number, 1.06; ratio of momentum thickness to nacelle diameter, 0.008; boundary-layer to free-stream velocity ratio, 1.064; boundary-layer to free-stream total pressure, 0.952.

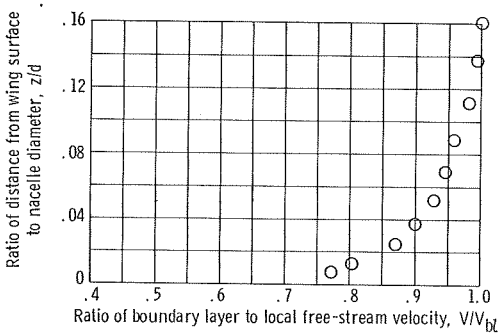

Flight Mach number, 1.19; ratio of momentum thickness to nacelle diameter, 0.008; boundary-layer to free-stream velocity ratio, 1.036; boundary-layer to free-stream total pressure, 0.957.

Figure 35. - Wing boundary-layer velocity profiles.

NATIONAL AERONAUTICS AND SPACE ADMINISTRATION
WASHINGTON, D. C. 20546

OFFICIAL BUSINESS

FIRST CLASS MAIL

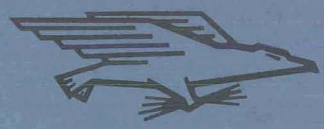

POSTAGE AND FEES PAID
NATIONAL AERONAUTICS AND
SPACE ADMINISTRATION

POSTMASTER: If Undeliverable (Section 158 Postal Manual) Do Not Return

"The aeronautical and space activities of the United States shall be conducted so as to contribute . . . to the expansion of human knowledge of phenomena in the atmosphere and space. The Administration shall provide for the widest practicable and appropriate dissemination of information concerning its activities and the results thereof."

— NATIONAL AERONAUTICS AND SPACE ACT OF 1958

NASA SCIENTIFIC AND TECHNICAL PUBLICATIONS

TECHNICAL REPORTS: Scientific and technical information considered important, complete, and a lasting contribution to existing knowledge.

TECHNICAL NOTES: Information less broad in scope but nevertheless of importance as a contribution to existing knowledge.

TECHNICAL MEMORANDUMS: Information receiving limited distribution because of preliminary data, security classification, or other reasons.

CONTRACTOR REPORTS: Scientific and technical information generated under a NASA contract or grant and considered an important contribution to existing knowledge.

TECHNICAL TRANSLATIONS: Information published in a foreign language considered to merit NASA distribution in English.

SPECIAL PUBLICATIONS: Information derived from or of value to NASA activities. Publications include conference proceedings, monographs, data compilations, handbooks, sourcebooks, and special bibliographies.

TECHNOLOGY UTILIZATION PUBLICATIONS: Information on technology used by NASA that may be of particular interest in commercial and other non-aerospace applications. Publications include Tech Briefs, Technology Utilization Reports and Notes, and Technology Surveys.

Details on the availability of these publications may be obtained from:

SCIENTIFIC AND TECHNICAL INFORMATION DIVISION

NATIONAL AERONAUTICS AND SPACE ADMINISTRATION

Washington, D.C. 20546